Mode-{I, III} multiaxial fatigue testing of high-quality welds in steel maritime structures using a hexapod

Bufalari, Gabriele; Troost, Niels; den Besten, Henk; Kaminski, Miroslaw Lech

DOI
10.1016/j.ijfatigue.2025.108870

Publication date
2025

Document Version
Final published version

Published in
International Journal of Fatigue

International Journal of Fatigue 197 (2025) 108870

Contents lists available at ScienceDirect

International Journal of Fatigue

journal homepage: www.elsevier.com/locate/ijfatigue

Mode-{I, III} multiaxial fatigue testing of high-quality welds in steel maritime structures using a hexapod

Gabriele Bufalari, Niels Troost, Henk den Besten *, Miroslaw Lech Kaminski

Maritime and Transport Technology Department, Delft University of Technology, Delft, The Netherlands

ARTICLE INFO

Keywords:
Fatigue
Multiaxiality
Welded joints
Hexapod
Effective notch stress
Total stress

ABSTRACT

Facing multiaxial fatigue testing challenges with respect to non-proportional loading conditions, a custom-built hexapod has been used to establish the mode-{I, III} resistance characteristics of high-quality welds in steel maritime structures. Assessment of the hexapod test data using the effective notch stress and total stress, respectively the best performing multiaxial intact and cracked geometry parameters, shows a fit in the reference quality literature data scatter band and provides conservative lifetime estimates. In order to improve the lifetime estimate accuracy, strength, geometry, material and mechanism aspects are investigated. Welding induced residual stress, a strength aspect, predominantly affects the mode-I fatigue resistance including a mean (residual) stress contribution. The weld notch radius, a geometry parameter, primarily influences the mode-III fatigue resistance. Similar material microstructure compositions of the high-quality welds and reference quality ones are observed, implying comparable mode specific mechanism parameters for the effective notch stress and total stress, respectively the material characteristic length and elastoplasticity coefficient. The material microstructure properties and classification criteria for high-quality welds support the residual stress estimates and suggest a smaller welding induced defect size. In general, the high quality is mainly reflected in the larger resistance curve intercept and slope, another strength and mechanism parameter, implying a larger initiation contribution to the total lifetime. For a high-quality resistance curve involving the representative strength, geometry, material and mechanism contributions, more accurate lifetime estimates are obtained, even though the parameter confidence is reduced because of the relatively small data size in comparison to the reference quality one.

1. Introduction

In order to validate the performance of multiaxial fatigue assessment concepts, test data is required. However, to introduce multiaxial structural response conditions into specimens – either loading, geometry and/or even material induced [1] – can be challenging with respect to test rig stiffness and stability, actuator control, specimen gripping as well as measurement system properties [e.g. 2] and may explain the limited availability of multiaxial fatigue test data for welded joints [3–6]. For geometry [e.g. 7–10] or material [e.g. 11] induced multiaxiality, uniaxial test rigs can still be used. To accelerate testing, ultrasonic technologies based on resonance can be employed [e.g. 12–14]. Non-proportionality, though, cannot be investigated – at least for metals like steel – and requires loading induced multiaxiality; i.e. multiple actuators [15] controlling different degrees of freedom (DoF's). Biaxial test rigs, involving either two translational DoF's or a combination of one translational and one rotational DoF, are nowadays standardised equipment, allowing respectively for mixed mode-{I, II} and mixed mode-{I, III} testing [e.g. 16–18]. For DoF's up to six, available test rigs are typically custom built for a particular purpose [e.g. 19–21].

Aiming for a wide application range and freedom with respect to specimen size and material strength, a high loading capacity six DoF multiaxial fatigue test rig, a hexapod (i.e. a Steward platform), has been developed. Whereas the typically available configurations with six linear actuators provide a combination of large motions and relatively small forces [e.g. 22,23], this one offers unparallelled performance in terms of loading combinations, accuracy, and system stability, allowing to investigate multiaxial fatigue of maritime structures [e.g. 24–26].

Available fatigue test data from literature, i.e. fatigue lifetime information N for a particular fatigue strength S, can be used to obtain reference quality based parameter coefficient estimates in order to establish one $S-N$ relation for general engineering applications [e.g. 27–29]. Depending on the specimen quality — reflected in strength, geometry, material and mechanism aspects; respectively welding induced residual stress, weld dimensions, as well as material microstructure composition and hardness distribution [e.g. 30–33], a particular data

* Corresponding author.
E-mail address: henk.denbesten@tudelft.nl (H. den Besten).

https://doi.org/10.1016/j.ijfatigue.2025.108870
Received 19 November 2024; Received in revised form 16 January 2025; Accepted 8 February 2025
Available online 18 February 2025

Nomenclature

Symbols

$\beta(N)$	lifetime dependent shear strength coefficient
γ	response ratio coefficient
Δ	prefix indicating stress range
λ_ω	width of spectrum
μ_ω	mean value of spectrum
ρ	(real) weld notch radius
ρ^*	material characteristic length
σ	normal stress
σ_{fe}	mode-I linear structural field stress
σ_N	fatigue lifetime standard deviation
$\sigma_n\ (r/t_p)$	weld toe notch stress distribution
$\sigma_{n,max}$	mode-I max. nominal stress after cut off
σ_s	(structural) normal stress
σ_{se}	mode-I self equilibrium stress
σ_{sb}	M_b induced structural normal stress component
σ_{sm}	F_n induced structural normal stress component
τ	shear stress
τ_{fe}	mode-III linear structural field stress
$\tau_n\ (r/t_p)$	mode-III weld toe notch shear stress distribution
$\tau_{n,max}$	mode-III max. nominal shear stress after cut off
τ_s	(structural) shear stress
τ_{se}	mode-III self equilibrium stress
τ_{ss}	F_s induced structural shear stress component
τ_{st}	M_t induced structural shear stress component
$\boldsymbol{\Phi}$	parameter vector
ω	frequency component of spectrum
a	crack size
a_f	final crack size
a_i	initial crack size
C	fatigue resistance curve intercept
C_{np}	path characteristic non-proportionality coefficient
c_m	material characteristic non-proportionality coeff.
F_n	nodal normal force
F_s	nodal shear force
h_w	weld leg height
I_N	notch crack growth integral
K	stress intensity factor
l_w	weld leg length
m	fatigue resistance curve slope
M_b	nodal bending moment
M_t	nodal torsion moment
n	number of counted cycles/elastoplasticity coefficient
N	fatigue lifetime in number of cycles
r	radial coordinate
r_{σ_s}	structural normal stress ratio
r_{τ_s}	structural shear stress ratio
R	response ratio
R_r	response ratio including S_r
S	fatigue strength parameter
S_r	(mean) residual stress
S_e	Effective notch stress parameter
S_T	total stress parameter
t_b	base plate thickness
t_c	cross plate thickness
t_p	plate thickness
$T_{\sigma S}$	10%–90% strength scatter band index
Y_f	far field factor
Y_n	notch factor
$\mathcal{L}$	log-likelihood
$_I$	mode-I index
$_{III}$	mode-III index

Abbreviations

AW	as-welded
BM	base metal
CA	constant amplitude
DoF	degree of freedom
DS	double side
FE	finite element
FZ	fusion zone
HAZ	heat affected zone
MCF	mid-cycle fatigue, $N = O(10^4 \ldots 5 \cdot 10^6)$ cycles
NP	non-proportional
P	proportional
SIF	stress intensity factor
SR	stress-relieved
VA	variable amplitude

set may be on the scatter band lower or upper bound. For high-quality welds, the reference quality based $S-N$ relation may provide overconservative fatigue strength and lifetime estimates. A dedicated one might be a better option, reflecting the actual quality.

In order to assess the multiaxial fatigue resistance of high-quality welds for maritime structures, test results obtained using the TU Delft hexapod will be evaluated. Test rig properties as well as specimens information will be provided first (Section 2). Fitting in the reference quality literature data scatter band will be investigated for both the effective notch stress S_e [28] and total stress S_T [29], including a parameter confidence bound analysis (Section 3) in order to evaluate if quality dependent $\{S_e - N,\ S_T - N\}$ relations would be preferred, rather than one for all data.

2. Multiaxial fatigue tests

Since the TU Delft hexapod is quite different from existing ones, design requirements and capabilities will be revealed (Section 2.1). The specimens were developed for mixed mode-{I, III} fatigue investigations and will be discussed with respect to geometry aspects, material microstructure properties, welding procedure and parameters, as well as metallurgical analysis results including macro and micro observations and hardness measurement data in order to verify the high-quality at materials level (Section 2.2). Last but not least, the fatigue test results will be provided, including (mixed) mode-specific fracture surface characteristics (Section 2.3).

2.1. Hexapod description

Parallel manipulators offer a high loading capacity, excellent dynamic response characteristics and accurate positioning capabilities [34]. Using six linear actuators in pairs; i.e. in parallel, attached to a base and crossing over to a platform at three equidistant positions, introduces a hexapod (Fig. 1), able to apply (coupled, multiaxial) motions and loads in six DoF: three translations/forces and three rotations/moments, varying over time. All twelve connections are principally universal joints. Depending on the operation requirements the actuators are either electric or hydraulic controlled, based on inverse kinematics equations.

Hexapods used for simulation purposes of ship, car or airplane dynamics typically involve relatively large motions and smaller loads. However, mechanical testing comes along with relatively large loads and smaller motions, meaning the system requirements will be completely different. For ultimate and fatigue limit state as well as struc-

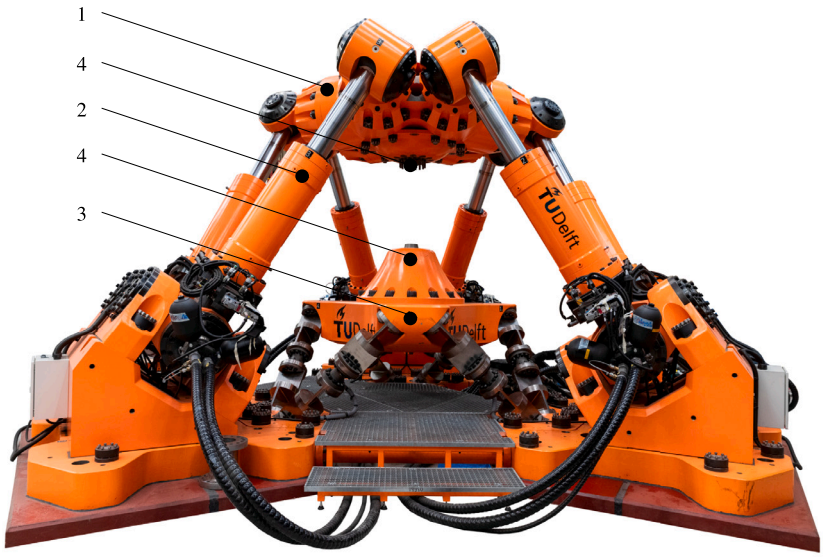

Fig. 1. TU Delft Hexapod. 1 = platform; 2 = actuator; 3 = pedestal with 6-DoF load cell; 4 = specimen grips.

Table 1
TU Delft hexapod dimensions and weight.

Item	Value
Diameter platform	2550 [mm]
Diameter cylinder lower attachment	4070 [mm]
Total height (neutral position)	3000 [mm]
Pedestal - platform distance (neutral position)	1200 [mm]
Pedestal - platform distance (max.)	1700 [mm]
Cylinder length (neutral position)	2080 [mm]
Cylinder stroke	±300 [mm]
Approximate platform weight	13 [tonnes]
Approximate total weight	60 [tonnes]

Table 2
TU Delft hexapod maximum load capacity.

description	capacity
Shear force	±400 [kN]
Shear displacement	±300 [mm]
Axial force	±1000 [kN]
Axial displacement	±450 [mm]
Bending moment	±400 [kNm]
Bending rotation	±11 [deg]
Torsion moment	±1000 [kNm]
Torsion rotation	±20 [deg]
Test frequency	0–30 [Hz]

tural dynamics testing at Delft University of Technology, a custom-built hydraulically controlled hexapod (Table 1) has been developed [35].

In order to be able to apply relative large loads (Table 2), i.e. forces up to 1 MN and moments up to 1 MNm, the system is operated using hydraulics with a max. oil flow capacity of 1500 L/min at 280 bar. Cyclic loading conditions up to 30 Hz can be both constant and variable (i.e. random). All DoF's can be individually controlled with respect to amplitude, frequency and phase. For measurement purposes, an advanced load cell in hexapod configuration has been developed, rather than a box type one. The six legs with predominant axial stiffness contain each an uniaxial load cell and the output is used to reconstruct the six DoF loads: three forces and three moments. The load cell deck is the pedestal the specimens can be mounted on. To fix the specimens, custom grips at the pedestal and/or platform are required.

For specimens in between the pedestal and platform, the maximum volume is about 1 m^3, allowing for larger sizes than typically fit in biaxial test rigs. Long slender specimens like pipe sections can be put through the platform and even through the pedestal, provided dedicated grips are used to enable mounting. Last but not least, specimens can be mounted on top of the platform, providing the possibility to investigate structural dynamics experimentally, like sloshing in LNG tanks or earth quake vibrations of buildings.

2.2. Specimen details

To investigate mode-{I, III} multiaxial fatigue of arc-welded double-sided T-joints, a tubular geometry rather than a planar one has been adopted (Fig. 2) to ensure the weld toe notch along the weld seam rather than at a weld seam end is governing. The selected base- and cross-plate thickness of 10 mm is representative for maritime structures. Flanges have been introduced to support bolt connections for specimen mounting purposes. In order to avoid a fatigue critical flange-tube transition, the curvature is quarter-elliptical.

Aiming for fixed boundary conditions, the specimens are fastened at each flange using 16 M20 double end threaded studs and super nuts with jack bolts for accurate pre-load control – up to 90% of the yield strength – without hydraulic tensioner. The stud normal strength and shear strength accommodate respectively the mode-I and mode-III specimen loading components. A diamond coated friction shim has been put in between the specimen flanges and the grips in order to prevent for mode-III torsion induced slip.

To make sure fatigue cracks will develop at the weld toe rather than the weld root, each specimen – consisting of a tube, two flanges and a circumferential attachment (Fig. 2) – is machined in one piece from a round bar of a commonly used steel grade in maritime structures: S355J2G3+N (Table 3). For reference purposes, the composition and properties of a similar type of grade; EH36, are provided as well. The yield strength for S355 is smaller than the tabular value and is likely a consequence of the bar manufacturing process, since the sample is taken from the representative pipe diameter location; i.e. away from the surface of the original round bar.

A partially penetrated fillet weld has been added at each side of the attachment to obtain the double-sided welded T-joint, with the weld starting ~180° away one from the other to make sure the two start and stop positions are not aligned. Although no thermal analysis has been performed, this precautionary measure is expected to prevent for concentration of thermal effects on a single side of each specimen. Welding a separate attachment to a tube would impose a

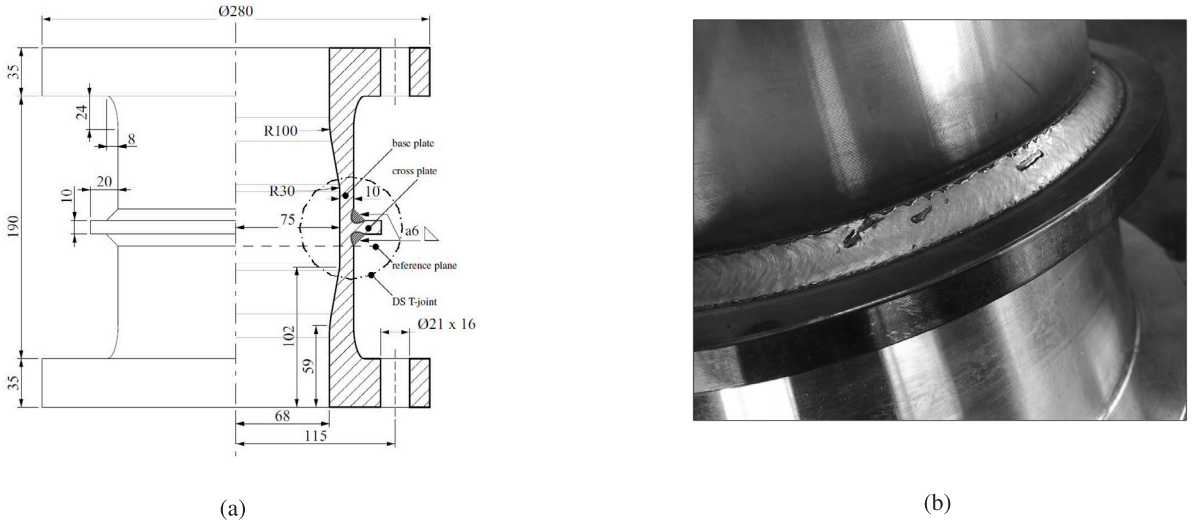

Fig. 2. Specimen geometry dimensions in [mm] with cross-sectional area $A_n = 5.0266 \cdot 10^3$ [mm^2], bending section modulus $Z_b = 1.8997 \cdot 10^5$ [mm^3] and torsion section modulus $Z_t = 3.7995 \cdot 10^5$ [mm^3] in the welded DS T-joint reference plane (a) and weld detail (b).

Table 3
Chemical composition information and mechanical properties of S355J2G3+N and EH36 steel, obtained using X-ray diffraction, combustion analysis and a tensile test.

Material	C	Si	Mn	P	Cr	Mo	Ni	Al	Cu
	[%]	[%]	[%]	[%]	[%]	[%]	[%]	[%]	[%]
S355	0.17	0.33	1.43	0.016	0.06	0.03	0.17	0.05	0.09
EH36	0.12	0.42	1.39	0.011	0.03	–	–	–	–

Material	Yield strength [MPa]	Tensile strength [MPa]	Young's modulus [GPa]
S355	340	506	206
EH36	406	548	206

Table 4
Mean μ and standard deviation σ of the measured weld dimensions in [mm].

Weld dimensions	l_w		h_w		ρ	
	μ	σ	μ	σ	μ	σ
Reference specimen	4.88	0.49	5.20	0.23	1.27	0.43
Hexapod specimen	9.16	0.44	9.06	0.44	3.12	0.99

full penetration requirement, meaning a significantly increased heat input, welding induced deformations as well as residual stresses and has been prevented for. The welds are fabricated using a robot, involving a turning manipulator and a fixed welding torch (Fig. 3).

The welding procedure has been certified according to quality standards (EN 10204-2004). Aiming for demanding offshore applications, visual and magnetic particle inspections (NEN-EN-ISO 17637 and 17638) yield the required acceptance criteria: respectively class B and level 2X (NEN-EN-ISO 5817 and NEN-EN-ISO 23278) reflecting high quality. A few specimens have been thermally stress-relieved at 560 – 600 °C for a minimum of 2 h to be able to get an impression of welding induced residual stress affecting the fatigue performance in comparison to the as-welded specimen data.

Optical microscopy as well as hardness measurement data are compared for the hexapod specimen welds with respect to the reference ones to illustrate the high-quality properties. For both welds, two samples were extracted from different specimens at different locations along the weld seam. The samples were cold mounted in a two-part acrylic resin and a range of P180 to P4000 grit sandpaper as well as 3 to 1 μm diamond polishing suspensions were used to prepare the metallurgical investigations. Nital 5% etchant was used for 5 s in order to reveal the microstructure.

Macro images were taken at 40x magnification using a microscope and stitched together to an image containing the complete weld. For both the reference and hexapod specimen welds, the base metal (BM); respectively EH36 and S355J2G3+N, the fusion zone (FZ) and the heat affected zone (HAZ) can be distinguished (Fig. 4). The weld dimensions were measured optically for 10 samples; i.e. weld leg length l_w, weld leg height h_w, as well as notch radius ρ using the base plate surface and idealised fillet weld as tangential lines (Table 4). The reference specimen weld notch radius turned out to be similar to previous observations [e.g. 36–38] and the hexapod specimen one seems relatively large, reducing the stress concentration.

Vickers hardness measurements were conducted using a DuraScan Microhardness Tester applying 2 kgf; HV2, rather than 5 kgf; HV5, or 10 kgf; HV10, in order to obtain sufficient spatial resolution (Fig. 5). Although in general the material zones of a perfect welded joint would have a homogeneous hardness distribution of similar magnitude as the BM, the actual distribution varies since the arc-welding induced heat input and cooling down process changes the material microstructure. Hardness distributions can be used to identify peak locations reflecting brittle spots (affecting the material toughness) and to provide information about fatigue influence factors like residual stress [e.g. 31].

The BM hardness for both welded joints is similar as expected, on average respectively 159 HV2 and 170 HV2. Increased hardness is observed in the FZ. For the reference specimen weld 328±15 HV2 left and 284±14 HV2 right (Fig. 5a), quite high and scattered values implying a rather inhomogeneous material structure. However, the hexapod specimen weld hardness of 222±4.0 HV2 left and 226±3.9 HV2 right (Fig. 5b) is relatively low and the standard deviation suggests a rather homogeneous one. The HAZ contains the highest hardness for both the reference and hexapod specimen weld, respectively 413 HV2 (Fig. 5a) and 343 HV2 (Fig. 5b). Note that the reference specimen weld value exceeds the allowed maximum of 380 HV10 (NEN-EN-ISO 9015-1:2011), keeping in mind that a HV2 maximum would be higher.

The hexapod specimen welded joint is more sensitive to the formation of hard brittle phases because of the relatively large {C, Mn, Si} content [39] of both the filler wire (Table 5) and the BM (Table 3). Since the same shielding gas (80%Ar + 20%CO_2) was used for welding

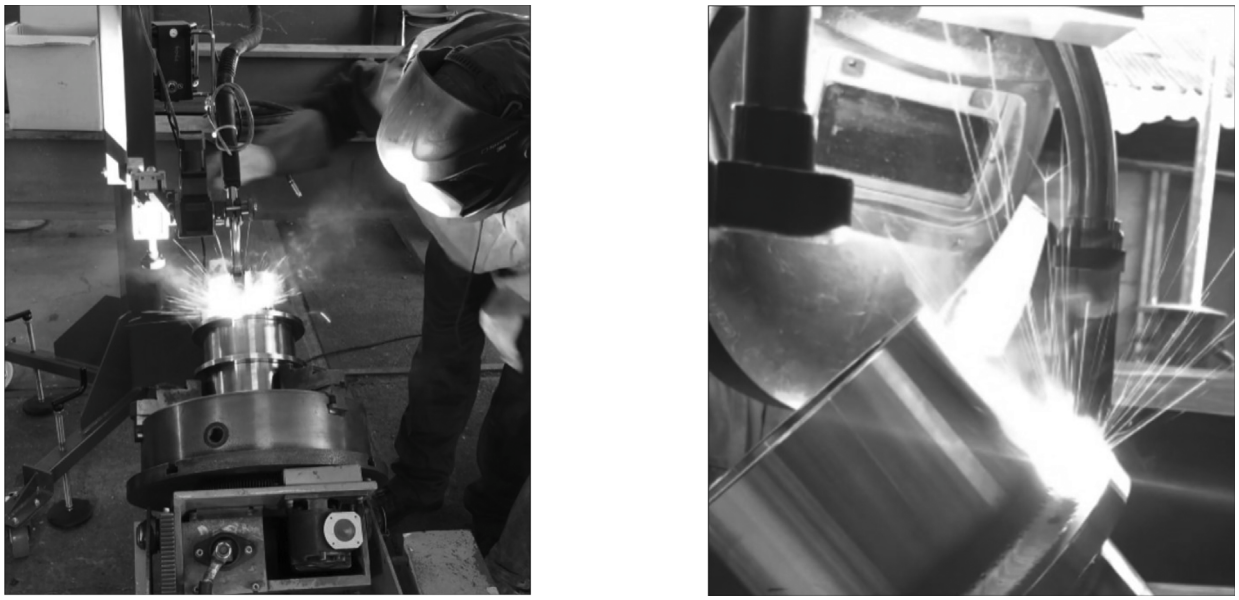

Fig. 3. Specimen welding using a robot with a turning manipulator and a fixed torch.

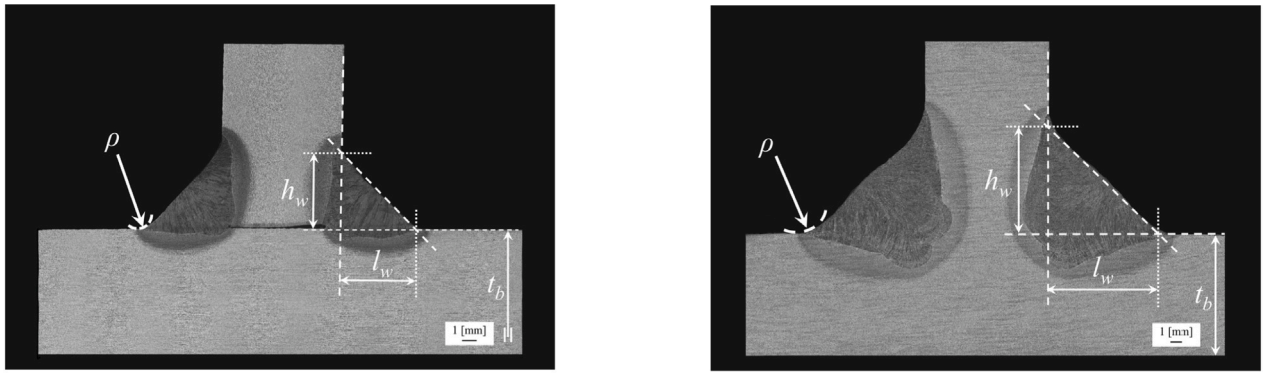

Fig. 4. Macro images for the reference (a) and hexapod (b) specimen welds.

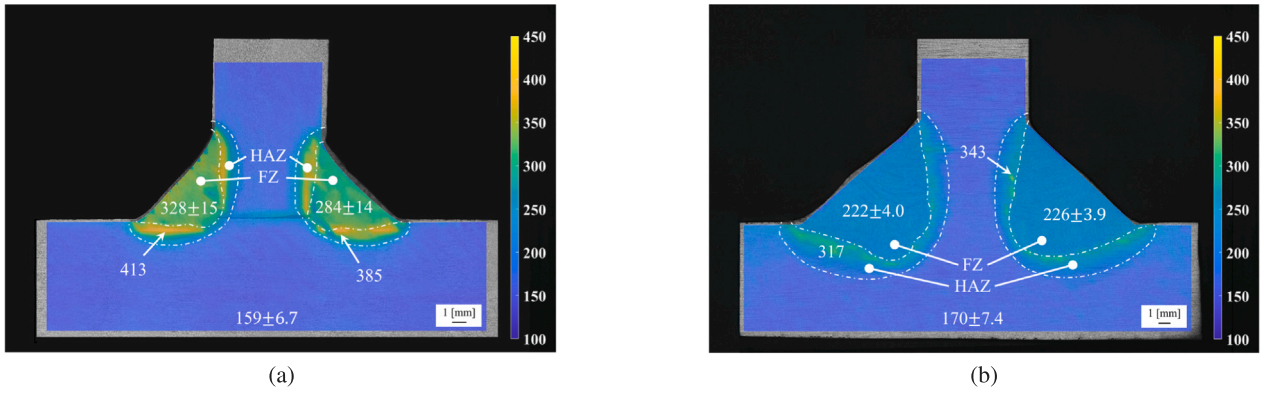

Fig. 5. Vickers hardness maps for the reference (a) and hexapod (b) specimen welds.

both joints as well, the weld dimensions and (welding parameter induced) penetration level are the most reasonable explanation for the obtained material microstructure, although no heat input nor cooling rate information is explicitly available. For a larger weld and deeper penetration level, more thermal energy needs to dissipate into the surrounding material, suggesting a lower cooling rate and a more gradual transition from one material zone to another (Figs. 4 and 5), typically responsible for reduced residual stress levels as well as smaller welding induced defects [e.g. 40].

Optical microscopy observations at high magnification (Fig. 6) and hardness map interpretations revealed that for the reference specimen weld the BM consists of ferrite (α) with a grain size of approximately

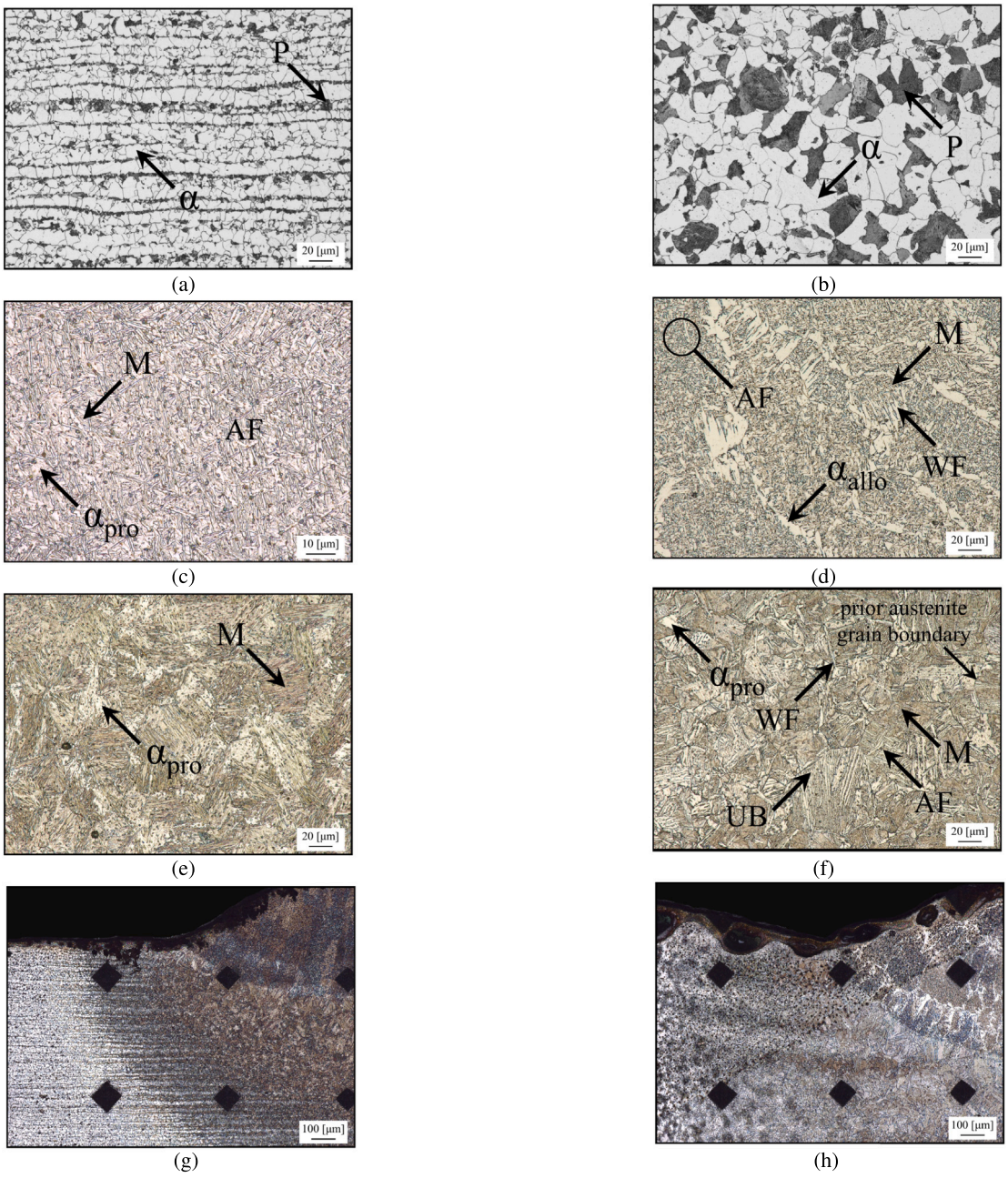

Fig. 6. Reference (left column) and hexapod (right column) specimen weld material microstructure for the BM (a and b), the HAZ (c and d), the FZ (e and f) and notch detail (g and h), showing ferrite (α), pearlite (P), proeutectoid ferrite (α_{pro}), allotriomorphic ferrite (α_{allo}), Widmanstätten ferrite (WF), acicular ferrite (AF), upper bainite (UB) and martensite (M).

Table 5
Chemical composition of weld filler materials.

Filler composition	Trade name	C [%]	Mn [%]	Si [%]
Reference specimen	ESAB PZ 6113	0.06	1.20	0.40
Hexapod specimen	Hyundai SM-70	0.08	1.47	0.83

10 µm and pearlite (P) in a banded structure, typical for rolled plates (Fig. 6a), whereas for the hexapod specimen weld ferrite with a grain size of approximately 20 µm and pearlite in a homogeneous structure is identified (Fig. 6b). The larger BM hardness of the hexapod specimen weld with respect to the reference one is a result of the increased carbon content (Table 3). Characterising the reference specimen weld FZ, predominantly acicular ferrite (AF) with proeutectoid ferrite (α_{pro}) and islands of martensite (M) are observed (Fig. 6c), while for the hexapod specimen weld FZ acicular ferrite, allotriomorphic ferrite (α_{allo}), Widmanstätten ferrite (WF) and limited formations of martensite (Fig. 6d) are discovered. The peak hardness in the HAZ of the reference specimen weld relates mostly to martensite with proeutectoid ferrite grains (Fig. 6e) and the one of the hexapod specimen weld to martensite, upper bainite (UB), acicular ferrite, proeutectoid ferrite and Widmanstätten ferrite forming directly from the prior austenite grain boundaries (Fig. 6f). The near-surface microstructure at the notch of the reference specimen weld (Fig. 6g) is very inhomogeneous as a result of the sharp FZ to BM transition, whereas for the hexapod specimen weld a more gradual change in microstructure is observed as a consequence of the thermal history (Fig. 6h). Although the near-surface hardness at the notch of the reference specimen weld is relatively large in comparison to the one of the hexapod specimen (Fig. 5) – suggesting an increased

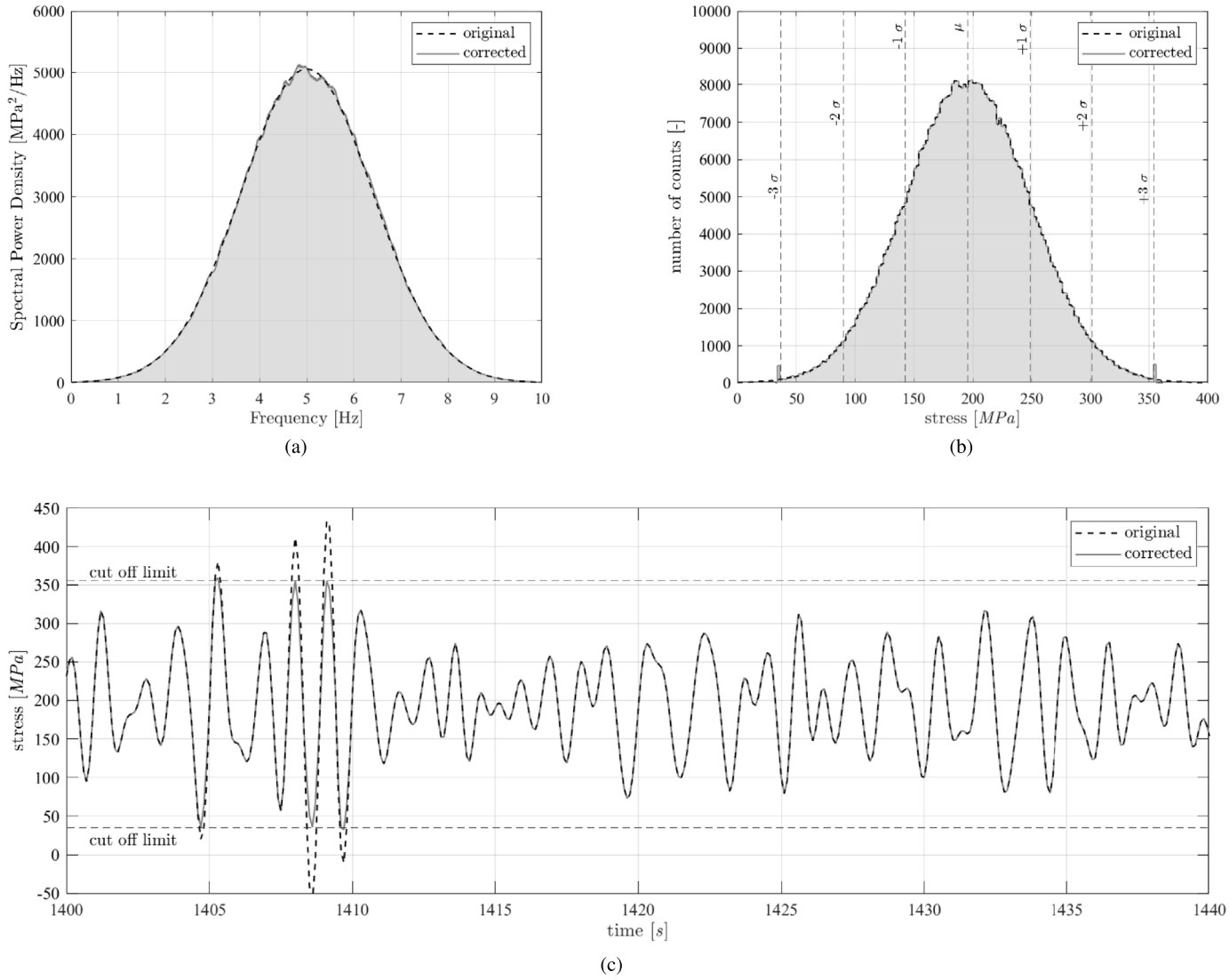

Fig. 7. Description of the Gaussian load sequence for the VA mode-I bending moment M_b test with $\Delta\sigma_{n,max}$ = 320 [MPa]. Gauss distributed frequency spectrum (a), histogram of counted cycles (b) and time trace (c). Original and corrected (after cutting off the extreme values).

fatigue crack initiation performance [e.g. 41], the short and long crack growth mechanism [e.g. 42] is most likely in charge because of the typical welding induced defects, flaws [e.g. 43,44].

2.3. Test program information and results

The 72 available specimens were used to generate uniaxial mode-I and mode-III as well as mixed mode-{I, III} data for both constant amplitude (CA) and variable amplitude (VA) loading in as-welded (AW) and in stress-relieved (SR) conditions, aiming to investigate multiaxial fatigue resistance including damage accumulation and mean (residual) stress aspects (Appendix).

Uniaxial CA data is acquired first to establish the mode-I and mode-III characteristics. Because of the tubular specimen geometry with a circumferential weld, mode-III data (15 specimens) were obtained (Fig. 8) applying a cyclic (sinusoidal) torsion moment M_t rather than a shear force F_s. Although fatigue induced failure may appear at the start/stop location, affecting the fatigue resistance, the actual locations were observed along the weld seam. The structural stress concentration factor $K_s = \tau_s/\tau_n$ is obtained using a solid finite element (FE) model and equals 1.05. Loading and response ratio $R_{III} = M_{t,min}/M_{t,max} = \tau_{min}/\tau_{max}$ is −1 to obtain a sufficiently high far field stress range (below yielding) for lifetimes in the mid-cycle fatigue (MCF) region: $N = O(10^4 \ldots 5 \cdot 10^6)$ cycles. Mode-I data (22 specimens) is obtained (Fig. 8) applying for the first few specimens a normal force F_n and for the remaining ones a bending moment M_b. Although F_n was preferred in order to avoid a weld volume effect [e.g. 45–47] and allow for a one-to-one comparison to the mode-III data, fatigue induced failures were obtained at the start/stop location. A M_b type of load with the start/stop location around the neutral axis turned out to be a solution, accepting that a possible weld volume effect may have to be taken care of. The structural stress concentration factor for F_n and M_b, $K_s = \sigma_s/\sigma_n$, is respectively 1.15 and 1.20. Loading and response ratio $R_I = F_{n,min}/F_{n,max} = M_{b,min}/M_{b,max} = \sigma_{min}/\sigma_{max}$ is 0.1 to obtain at least a fully effective far field response cycle as far as the applied $\{F_n, M_b\}$ is concerned, assuming that mode-III mean stress effects are typically negligible [1,28,29] and a mode-I to mode-IIII data comparison is still feasible. To indicate any mean (residual) stress effect, some tests have been conducted with $R_I = -1$, involving both AW and SR specimens (Fig. 8).

Mixed mode-{I, III} CA data is obtained applying $\{M_b|R_I = 0.1, M_t|R_{III} = 0.1\}$ simultaneously, either proportional (P): in-phase, non-proportional (NP): 90 [deg] out-of-phase, or with a frequency ratio of 1 : 3 meaning for 1 cycle in bending 3 cycles in torsion are applied

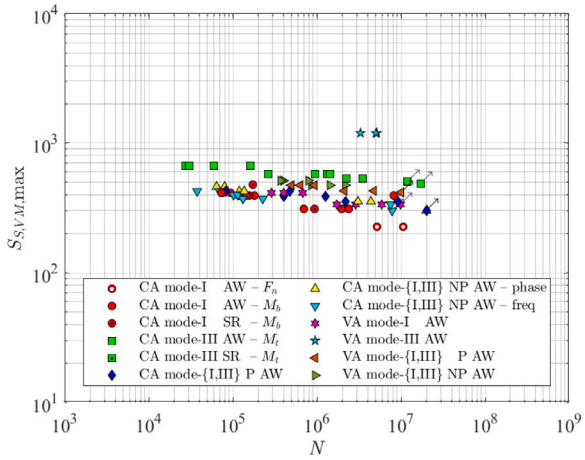

Fig. 8. Hexapod fatigue test data.

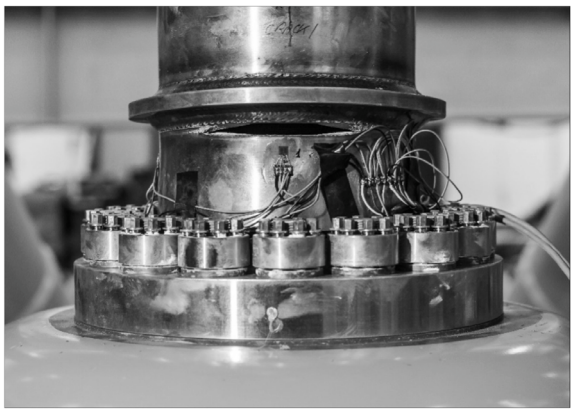

Fig. 9. Specimen in hexapod after fatigue failure with through-thickness crack.

at the same time. Based on the von Mises type of criterion [28,29], $\tau = \sqrt{3}\sigma$ has been adopted to ensure equal nominal shear and normal stress contributions to failure [35].

For both the uniaxial and multiaxial random VA loading and response conditions, the generated time traces are based a on Gauss distributed frequency spectrum (Fig. 7): $G(\omega) = (\Delta S_{n,max}/6)^2 \cdot \exp\{-(\omega - \mu_\omega)^2/(2 \cdot \lambda_\omega^2)\}/\{\sqrt{2\pi}\lambda_\omega\}$, with $\Delta S_{n,max}$ a nominal normal or shear stress range scaling parameter, the spectrum width $\lambda_\omega = 1.4$ and the spectrum mean value $\mu_\omega = 5$. For the uniaxial mode-{I, III} VA conditions the time trace global mean $\{R_I, R_{III}\}$ is $\{0.1, -1\}$, similar to the CA values. The $\tau(t)$ and $\sigma(t)$ time series for the mixed mode-{I, III} VA conditions are the same, except for the von Mises based scaling of the magnitude and the 90 [deg] phase shift for the NP conditions. Like for the CA case, the time trace global mean $\{R_I, R_{III}\}$ is $\{0.1, -1\}$.

To make sure sufficient statistical variability is accounted for [48], the time trace length is $5 \cdot 10^4$ cycles. However, the length is relatively large and the time trace may contain extremes at a very small probability of occurrence, but should be prevented for to avoid yielding. A clipping ratio has been introduced to cut off the extremes exceeding 3 times the time trace standard deviation; both the maxima and the minima (Fig. 7). Since the global mean value of the generated time traces is zero; i.e. $R = -1$, a shift is applied if $R = 0.1$ is required. The time trace irregularity factor I_r, defined as the ratio of the number of zero up-crossings and the number of peaks, a bandwidth measure, has been set to $I_r = 0.88$ and resembles a typical wave irregularity encountered by maritime structures

A von Mises based structural stress range vs. lifetime $S_{s,VM,max} - N$ plot (Fig. 8) of the obtained test results (Tables A.9 and A.10) shows the initial fatigue resistance data scatter. Distinct strength and mechanism contributions can be observed comparing uniaxial mode-I and mode-III results for both CA and (maximum range $S_{s,VM,max}$ signed) VA loading conditions. The mode-I F_n and M_b results are not very well aligned and might be a consequence of volume effects and/or failures at the start/stop location. Even the different notch stress gradients could provide a contribution. At first glance, the uniaxial AW and SR mode-{I, III} data does not show a significantly different fatigue strength, suggesting a residual stress might not be involved at all in support of the material microstructure properties (Section 2.3). The uniaxial mode-I and mixed mode-{I, III} test data seems to align; similar to literature data [28]. Note that N for the multiaxial data is based on the mode-I contribution only, since no multiaxial cycle counting is involved. Mean stress effects are not incorporated and may partially explain why the mode-III data tested at $R = -1$ shows a relatively large fatigue strength in comparison to the other data obtained at $R = 0.1$. The $S_{s,VM,max}$ value for the mode-III VA data exceeds the yield strength. Avoiding structural stress cycles with an elastoplastic response was preferred, but turned out to be inevitable because of the aim to obtain failures in the MCF region.

As soon as a semi-elliptical through-thickness crack has developed at the position of the fabrication induced weakest link along the weld seam (Fig. 9); the adopted failure criterion, FE calculation based max displacement and rotation values are reached and the fatigue test is stopped, defining the corresponding number of cycles N. A quasi-static increase of the crack opening afterwards allows for fracture surface observations and distinct patterns can be distinguished (Fig. 10). Some highlights will be addressed.

The fracture surfaces for the mode-I CA and VA data turned out to be relatively smooth, similar, as well as loading and response level invariant. A crack with a semi-elliptical shape has grown in through-thickness direction (Fig. 10a and b). For the mode-III CA and VA data, the fracture surface characteristic pattern appeared to be loading and response level dependent. At higher load level (Fig. 10c), the crack developed straight along the weld seam and looks similar to the mode-I equivalent. Reducing the load level (Fig. 10d), the characteristic V (for $R_{III} > 0$) or X ($R_{III} < 0$) shapes tend to become more apparent [e.g. 49,50]. Differences for CA and VA did not seem significant. Mixed mode-{I, III} P CA and VA loading and response conditions come along with mixed fracture characteristic contributions. Comparing the crack surfaces for higher (Fig. 10e) and lower (Fig. 10f) load levels, a mode-III induced load level dependency is observed and the V or X shapes can be distinguished more and more clearly. Although mixed mode-{I, III} characteristic fracture contributions can still be identified for the NP CA and VA loading and response conditions, including a mode-III induced load level dependency (Fig. 10g and h), the mode-I contribution is more dominant than observed for the mixed mode-{I, III} P crack surfaces (Fig. 10e and f). The fracture surfaces for the mixed-mode-{I, III} P $\sigma : \tau = 1 : 3$ ratio shows the mode-III induced load level dependent characteristics as well (Fig. 10i and j). Note that the extent of the V or X shaped pattern is observed to be in between the ones of the uniaxial mode-III and multiaxial mode-{I, III} P conditions (Fig. 10d, f and i); a frequency effect.

Last but not least, the fatigue lifetime standard deviation σ_N, a scatter measure, of the individual uniaxial and multiaxial $S_{s,VM,max} - N$ data series (Fig. 8) correlates roughly speaking to the contribution of the mode-III induced X or V shaped characteristic to the fracture surface pattern (Fig. 10); i.e. the more pronounced, the larger σ_N (Table 6). Results are obtained using maximum likelihood regression for a single slope formulation: $\log(N) = \log(C) - m \cdot \log(S_{s,VM,max})$, considering failures only and ignoring run-outs.

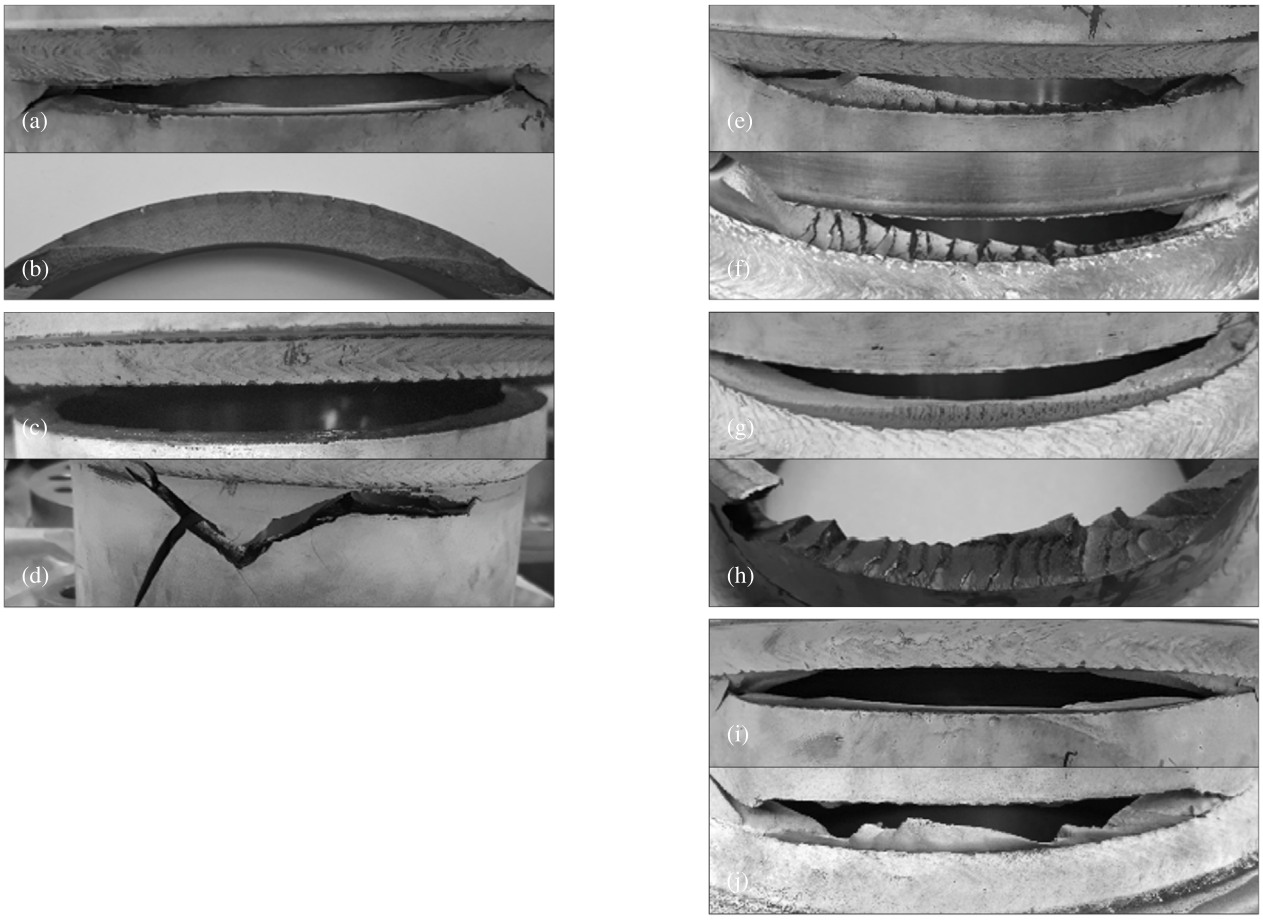

Fig. 10. Fracture surface characteristics for mode-I (a, b), mode-III (c, d), mixed mode-{I, III} P (e, f), mixed mode-{I, III} NP (g, h), mixed mode-{I, III} P with frequency ratio $\sigma : \tau = 1 : 3$ (i, j).

Table 6
Fatigue lifetime standard deviation σ_N for individual $S_{s,VM,max} - N$ data series.

Load case	σ_N
Mode-I	0.15
Mode-III	0.33
Mode-{I, III} P	0.32
Mode-{I, III} NP – phase	0.13
Mode-{I, III} NP – frequency	0.13

3. Multiaxial fatigue assessment

The fatigue damage process involves an initiation and growth contribution [51] and can be modelled using a fatigue strength parameter S in order to obtain a lifetime estimate N [52]. Since far field response spectra of welded joints in steel maritime structures reflect predominantly linear elastic behaviour, S is typically of the stress – rather than strain or energy – type, in particular for mid- and high-cycle fatigue [27]. Correlation of S and N in the MCF region often reveals a log–log linear relation and a Basquin type of formulation is naturally adopted: $\log(N) = \log(C) - m \cdot \log(S)$; a resistance curve. Intercept $\log(C)$ and slope m are respectively mode specific and material characteristic strength and damage mechanism coefficients. Using maximum likelihood based regression on fatigue lifetime, $\max\{\mathcal{L}(\boldsymbol{\Phi}; N|S); \boldsymbol{\Phi}\}$, introduces the lifetime standard deviation and scatter measure σ_N [53,54] and the most likely parameter vector estimate $\boldsymbol{\Phi} = \{\log(C), m, \sigma_N\}$ can be obtained. The lifetime N in the MCF region is assumed to be Log-Normal distributed [1,55]. Scatter band index $T_{\sigma S} = 1 : (S_{10}/S_{90})$, the fatigue strength ratio for 10% and 90% probability of survival [56] is adopted for strength performance evaluation purposes.

A major part of the fatigue damage is accumulated in the notch affected region [e.g. 57], suggesting the fatigue strength parameter S could be a notch characteristic intact geometry parameter like the effective notch stress S_e [28]. At the same time, the notches typically contain welding induced defects [e.g. 37]. The actual initiation (i.e. nucleation) contribution to the total fatigue lifetime is virtually eliminated and growth is governing, suggesting a cracked geometry parameter like the total stress S_T incorporating the notch characteristics seems justified as well [29].

For mixed mode-{I, III} multiaxial response conditions of planar and tubular (maritime) structures, the mode-I contribution is governing [28,29]. The normal stress is predominant, explaining why a mode-I equivalent normal stress based von Mises type of failure criterion:

$$S_e = \sqrt{S_{e,I}^2 + \beta(N) S_{e,III}^2} \tag{1}$$

or

$$S_T = \sqrt{S_{T,I}^2 + \beta(N) S_{T,III}^2}\,, \tag{2}$$

is adopted. Rather than a constant shear strength coefficient, a lifetime dependent one:

$$\beta(N) = C_\beta \cdot N^{M\beta} \tag{3}$$

with

$$C_\beta = 10^{[\log(C_I)\cdot m_{III} - \log(C_{III})\cdot mI]/[m_I \cdot m_{III}]}$$

and

$$M_\beta = (m_I - m_{III})/(m_I \cdot m_{III}),$$

has been introduced to cover the mode-{I, III} strength and mechanism contributions $\{\log(C_I), \log(C_{III}), m_I, m_{III}\}$ for welded joints in steel structures [28,29].

Since cracks at weld notches typically develop first in plate thickness direction, the fracture plane is identified as the decisive one and is selected for criterion evaluation. Cycles are counted – adopting a time domain approach – in the von Mises $\{S_{e,I} - \beta(N) \cdot S_{e,III}\}$ or $\{S_{T,I} - \beta(N) \cdot S_{T,III}\}$ stress plane [28,29]. Using a 1st order moment formulation, differences between the actual response path and the (straight) range for each cycle i have been used to incorporate a cycle-by-cycle non-proportionality effect in terms of C_{np}, including a material characteristic contribution c_m:

$$S_{e,eff} = S_{e,i}(1 + c_m \cdot C_{np,i}) \tag{4}$$

or

$$S_{T,eff} = S_{T,i}(1 + c_m \cdot C_{np,i}). \tag{5}$$

In order to obtain an equivalent fatigue strength parameter for VA data fitting the mode-I CA data scatter band, a linear damage accumulation model is adopted. For damage $D = 1$ rather than a smaller value [28, 58,59] reflecting failure:

$$S_{e,eq} = \left[\sum\{n_i(S_{e,eff,i}) \cdot S_{e,eff,i}^{m_I}\}/N\right]^{1/m_I} \tag{6}$$

or

$$S_{T,eq} = \left[\sum\{n_i(S_{T,eff,i}) \cdot S_{T,eff,i}^{m_I}\}/N\right]^{1/m_I}. \tag{7}$$

Using S_e (Section 3.1) and S_T (Section 3.1), the uniaxial mode-I and mode-III resistance (Section 3.3) will be investigated first, before the mixed-mode-{I, III} fatigue characteristics will be established (Section 3.4). Particular attention will be paid to the strength and mechanism contributions, as well as the parameter coefficient confidence [e.g. 60] to be able to evaluate if quality dependent resistance curves or just one for all data would be preferred.

3.1. Fatigue strength parameter S_e

The through-thickness weld notch stress distributions along the expected (2D) crack path – defining the fracture plane – are assumed to be a key element for an appropriate fatigue design and repair criterion [55]: a through-thickness crack allowing for detection at visual inspection. Semi-analytical mode-{I, III} formulations $\{\sigma_n(r/t_p, \sigma_s), \tau_n(r/t_p, \tau_s)\}$, with plate thickness t_p either the base plate or cross plate value (Fig. 2a), t_b or t_c, have been developed for both non-symmetry and symmetry with respect to half the plate thickness ($t_p/2$), in case of both zero and finite notch radius ρ [1,55]. Adopting a linear superposition principle, far field related equilibrium equivalent and self-equilibrium parts $\{\sigma_{fe}, \sigma_{se}; \tau_{fe}, \tau_{se}\}$ have been distinguished, involving three components: the notch stress, the weld-load carrying stress and the far field stress. Typically three zones can be identified in all distributions: the zone 1 peak stress value, the zone 2 notch-affected stress gradient and the zone 3 far-field dominated stress gradient. Excellent performance is proven in comparison to FE solutions, like illustrated (Figs. 11a and b, 12a and b) for the fatigue specimen geometry (Section 2.2), meaning numerical modelling [e.g. 61] is not required to estimate the effective notch stress S_e.

Taking advantage of $\{\sigma_n(r/t_p, \sigma_s), \tau_n(r/t_p, \tau_s)\}$, S_e can be calculated averaging the notch stress distribution along the expected crack path over a material characteristic length ρ^*; another mechanism parameter. Uniaxial mode-I and mode-III investigations for welded joints in steel (maritime) structures revealed distinguished $\{\rho_I^*, \rho_{III}^*\}$ as well as $\{\log(C_I), \log(C_{III})\}$ and $\{m_I, m_{III}\}$ values [1,27,55]. Since a response cycle needs two parameters for a complete spatial description, e.g. range $S = (S_{max} - S_{min})$ and ratio $R = (S_{min}/S_{max})$, mode specific response ratio coefficients $\{\gamma_I, \gamma_{III}\}$; additional strength parameters, have been discovered as well to obtain an effective formulation [28]: $S_{e,eff} = S_e/(1 - R)^{1-\gamma}$. If both AW and SR test data are jointly considered, an explicit residual stress measure S_r has been introduced to cover the thermal condition, turning the ratio into: $R_r = (S_{e,min} + S_r)/(S_{e,max} + S_r) = \{R \cdot S_e + S_r(1 - R)\}/\{S_e + S_r(1 - R)\}$. Dedicated $\{\rho_{I,AW}^*, \rho_{I,SR}^*\}$ and $\{\gamma_{I,AW}, \gamma_{I,SR}\}$ mode-I contributions are established. The mean (residual) stress – reflected in R_r – hardly affects the mode-III fatigue resistance [28], explaining why no ratio contribution is involved. Coefficient $\gamma_{III} = 1$, regardless the thermal condition. For $S = S_e$, regression analysis provides the most likely extended parameter vector estimates $\Phi = \{\log(C), S_r, \gamma_{I,AW}, \gamma_{I,SR}, m_I, \rho_{I,AW}^*, \rho_{I,SR}^*, \rho_{III}^*, \sigma_N\}$ to obtain the mode-{I, III} effective notch stress contributions:

$$S_{e,I} = \frac{S_{e,I}}{(1 - R_{r,I})^{1-\gamma_I}} = \int_0^{\frac{\rho_I^*}{t_p}} \frac{\sigma_n\left(\frac{r}{t_p}, \Delta\sigma_s\right)}{(1 - R_{r,I})^{1-\gamma_I}} \mathrm{d}\left(\frac{r}{t_p}\right) \tag{8}$$

and

$$S_{e,III} = \int_0^{\frac{\rho_{III}^*}{t_p}} \tau_n\left(\frac{r}{t_p}, \Delta\tau_s\right) \mathrm{d}\left(\frac{r}{t_p}\right). \tag{9}$$

The involved far field stress information $\{\Delta\sigma_s, r_{\sigma s}; \Delta\tau_s, r_{\tau s}\}$ is calculated using nodal force output of relatively coarse meshed shell/plate FE models [62–64], providing the structural normal stress range: a superposition of a constant membrane and linear bending contribution: $\Delta\sigma_s = \Delta\sigma_{sm} + \Delta\sigma_{sb}$, as well as the structural shear stress range: $\Delta\tau_s = \Delta\tau_{ss} + \Delta\tau_{st}$, involving a constant shear and linear torsion contribution. The structural normal and shear stress ratios: $r_{\sigma s} = (\Delta\sigma_{sb}/\Delta\sigma_s)$ and $r_{\tau s} = (\Delta\tau_{st}/\Delta\tau_s)$ reflect the far field stress gradients [1,55].

3.2. Fatigue strength parameter S_T

Converting the intact geometry related weld toe notch stress distribution expressions into crack damaged equivalents [29], the zone {1, 2} self-equilibrium and zone 3 equilibrium equivalent stress parts $\{\sigma_{fe}(r/t_p), \sigma_{se}(r/t_p); \tau_{fe}(r/t_p), \tau_{se}(r/t_p)\}$ have been used to obtain respectively a notch factor $Y_n(a/t_p)$ and a far field factor $Y_f(a/t_p)$, defining the weld toe notch stress intensity factor (SIF) for respectively mode-I and mode-III: $K_I = \sigma_s\sqrt{t_p}Y_{n,I}(a/t_p)Y_{f,I}(a/t_p)\sqrt{\pi(a/t_p)}$ and $K_{III} = \tau_s\sqrt{t_p}Y_{n,III}(a/t_p)Y_{f,III}(a/t_p)\sqrt{\pi(a/t_p)}$. In comparison to FE solutions, excellent performance is proven for the semi-analytical stress intensity $\{Y_{n,I}Y_{f,I}, Y_{n,III}Y_{f,III}\}$ as well as the SIF $\{K_I, K_{III}\}$ formulations, like illustrated (Figs. 11c and d, e and f; 12c and d, e and f) for the fatigue specimen geometry (Section 2.2). Numerical modelling [66,67] is not required.

Cyclic loading induced response conditions turn the SIF's $\{K_I, K_{III}\}$ into crack growth driving forces $\{\Delta K_I, \Delta K_{III}\}$ and defects may develop into cracks. The crack growth rate ($\mathrm{d}a/\mathrm{d}n$) of short-cracks emanating at notches show elastoplastic wake field affected anomalies [53]. Modifying Paris' equation, a generalised two-stage model has been established containing a transition from a short to a long crack growth region meant to incorporate all relevant crack growth driving force components [68–70]; i.e. to include both the weld notch- and far field characteristic mode-{I, III} response contributions: $(\mathrm{d}a/\mathrm{d}n)_I = C_I \cdot Y_{n,I}^{n,I} \cdot \{\Delta\sigma_s \cdot Y_{f,I} \cdot \sqrt{\pi a}\}^{m_I}$ and $(\mathrm{d}a/\mathrm{d}n)_{III} = C_I \cdot Y_{n,III}^{n,III} \cdot \{\Delta\tau_s \cdot Y_{f,III} \cdot \sqrt{\pi a}\}^{m_I II}$. Notch elastoplasticity coefficients $\{n_I, n_{III}\}$; mechanism parameters, are response dependent and define the level of monotonically increasing or non-monotonic crack growth behaviour. For a complete spatial description, R_r has been introduced like for S_e, adding $\{\gamma_I, \gamma_{III}\}$ as strength parameters. Applying an integral operator on the individual mode-{I, III} crack growth models provides MCF related resistance relations of the Basquin type: $\log(N_I) = \log(C_I) - m_I \log(S_{T,I})$ and $\log(N_{III}) = \log(C_{III}) - m_{III} \log(S_{T,III})$, with the mode-{I, III} total stress contributions [29]:

$$S_{T,I} = \frac{S_{T,I}}{(1 - R_{r,I})^{1-\gamma_I}} = \frac{\Delta\sigma_s}{\left(1 - R_{r,I}\right)^{1-\gamma_I} \cdot I_{N,I}^{\frac{1}{m_I}} \cdot t_p^{\frac{2-m_I}{2m_I}}} \tag{10}$$

with

$$I_{N,I} = \int_{\frac{a_i}{t_p}}^{\frac{a_f}{t_p}} \frac{1}{\left\{Y_{n,I}\left(\frac{a}{t_p}\right)\right\}_I^n \cdot \left\{Y_{f,I}\left(\frac{a}{t_p}\right)\right\}_I^m \cdot \left(\frac{a}{t_p}\right)^{\frac{m_I}{2}}} \mathrm{d}\left(\frac{a}{t_p}\right)$$

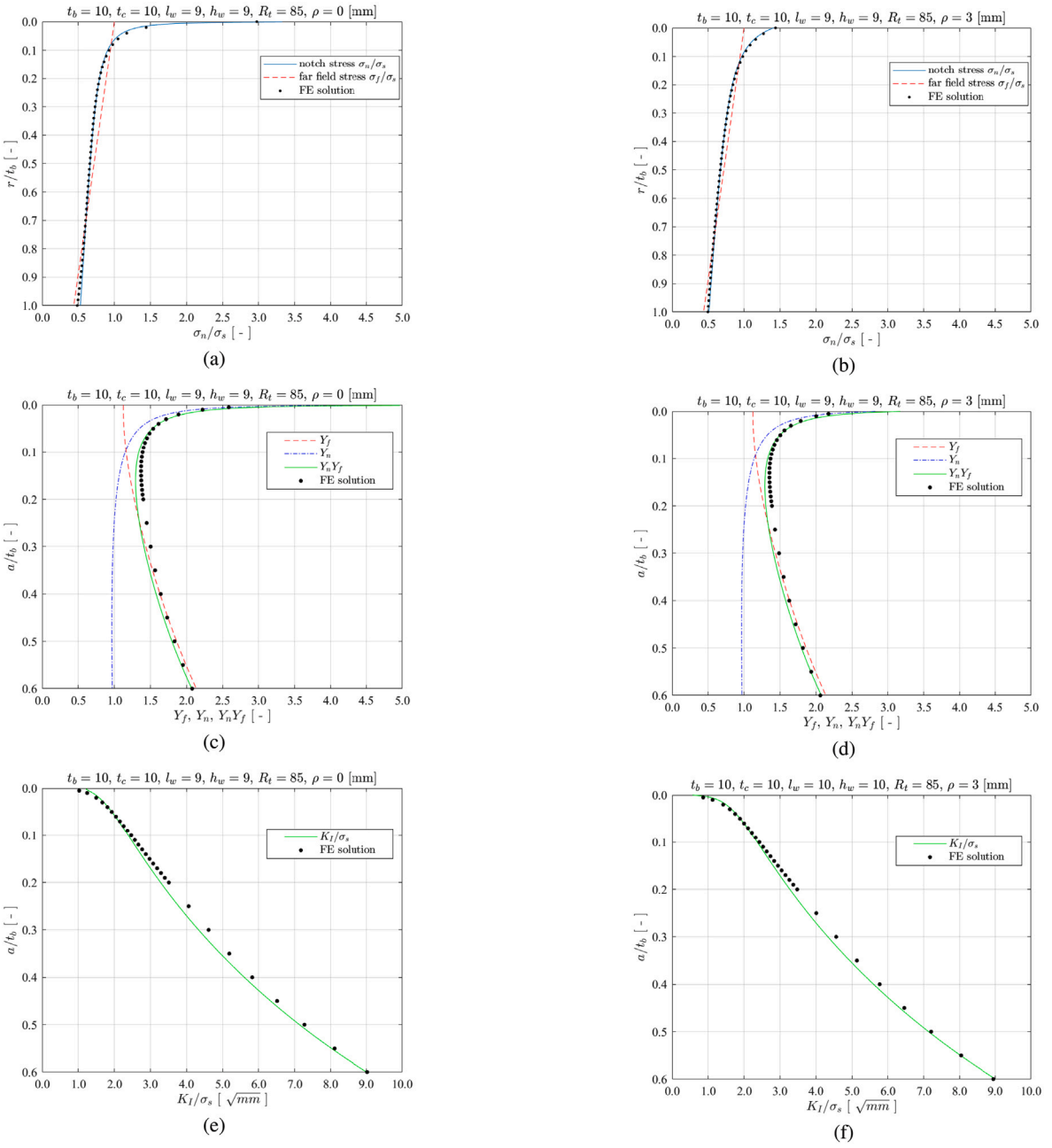

Fig. 11. Mode-I weld toe notch stress distributions (a, b), SIF far field- and notch distributions (c, d) and K_I distributions (e, f) for the specimen geometry (Fig. 2) with respectively $\rho = 0$ (a, c, e) in a worst case scenario and the measured $\rho = 3.0$ (b, d, f).

and

$$S_{T,III} = \frac{S_{T,III}}{(1 - R_{r,III})^{1-\gamma_{III}}} = \frac{\Delta\sigma_s}{\left(1 - R_{r,III}\right)^{1-\gamma_{III}} \cdot I_{N,III}^{\frac{1}{m_{III}}} \cdot t_p^{\frac{2-m_{III}}{2m_{III}}}} \tag{11}$$

with

$$I_{N,III} = \int_{\frac{a_i}{t_p}}^{\frac{a_f}{t_p}} \frac{1}{\left\{Y_{n,III}\left(\frac{a}{t_p}\right)\right\}_{III}^{n} \cdot \left\{Y_{f,III}\left(\frac{a}{t_p}\right)\right\}_{III}^{m} \cdot \left(\frac{a}{t_p}\right)^{\frac{m_{III}}{2}}} \mathrm{d}\left(\frac{a}{t_p}\right).$$

Regression analysis provides the most likely extended parameter vector estimates: $\Phi = \{\log(C),\ S_r,\ \gamma_{I,AW},\ \gamma_{I,SR},\ m_I,\ n_{I,AW},\ n_{I,SR},\ n_{III},\ \sigma_N\}$. Thermal conditions require distinguished mode-I elastoplasticity coefficients $\{n_{I,AW}, n_{I,SR}\}$. Mode-III mean (residual) stress effects are insignificant, explaining $\gamma_{III} = 1$. Scaling parameters $\{t_p^{(2-m_I)/(2m_I)}, t_p^{(2-m_{III})/(2m_{III})}\}$ take the response gradient induced size effects into account. Rather than a sufficiently small welding induced defect size (a_i/t_p) providing a converged notch crack growth integral solutions $\{I_{N,I}, I_{N,III}\}$, an arc-welding induced most likely material characteristic estimate has been established; $(a_f/t_p) = 1$ is based on a through-thickness crack criterion.

3.3. Uniaxial resistance

The S_e based uniaxial mode-I MCF reference resistance for planar and tubular geometries in steel (maritime) structures, involving both AW and SR thermal conditions, has already been established for CA and VA literature data [28,55].

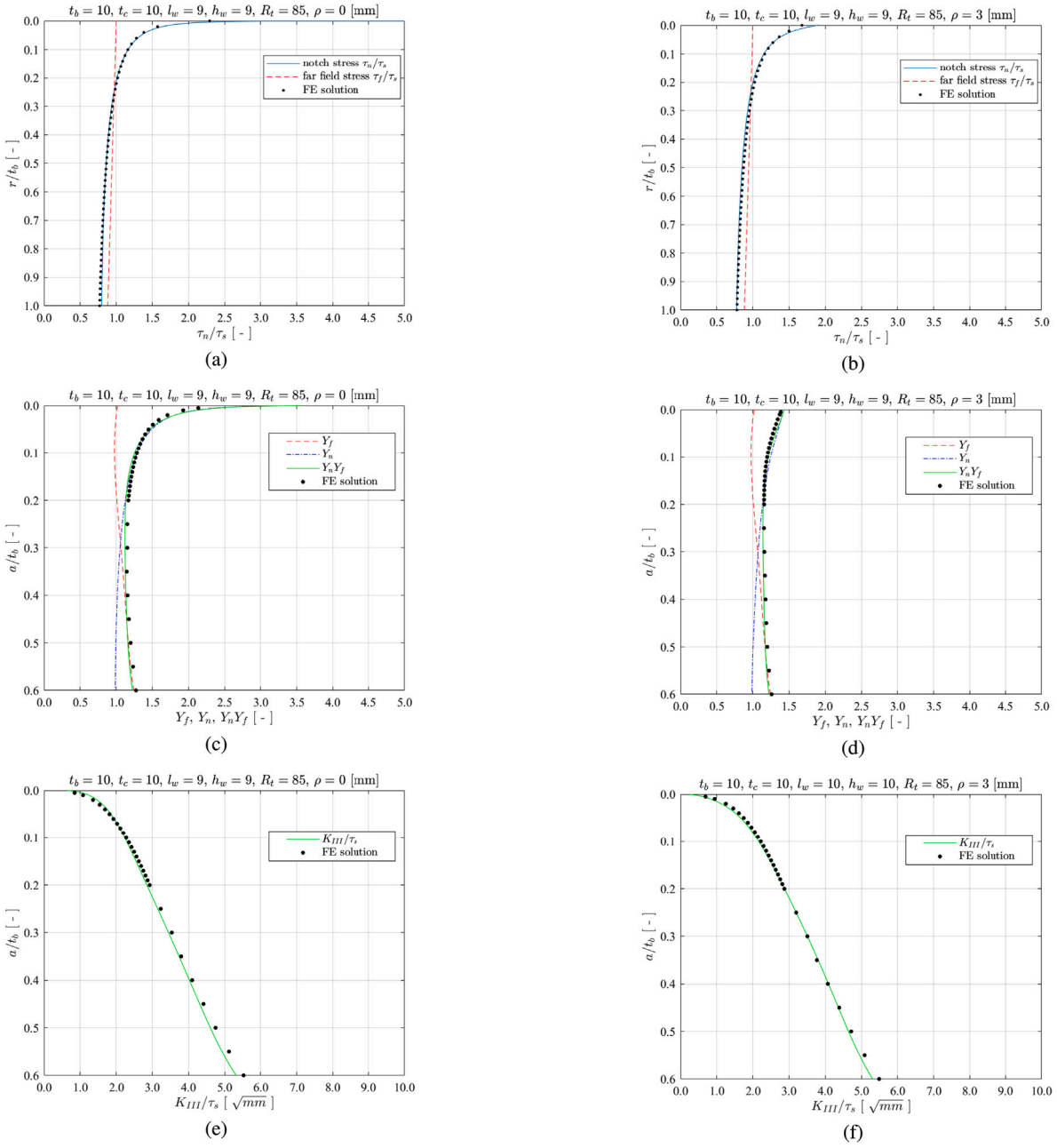

Fig. 12. Mode-III weld toe notch stress distributions (a, b), SIF far field- and notch distributions (c, d) and K_{III} distributions (e,f) for the specimen geometry (Fig. 2) with respectively $\rho = 0$ (a, c, e) in a worst case scenario and the measured $\rho = 3.0$ (b, d, f).

In order to fit for tubular geometries the SR literature data in the AW literature data scatter band, a residual stress component S_r – a strength related quality aspect – has been introduced. Since the AW thermal condition is considered to be the reference case for fatigue design, S_r is applied to the SR data explaining the compressive value [28]. However, in contrast to the literature data, the fatigue strength of the AW and SR hexapod data is similar (Fig. 8), suggesting that no residual stress is involved at all. To fit the MCF hexapod data into the literature data scatter band, S_r should apply for both the AW and SR thermal conditions. Adopting the most likely reference parameter estimates for regression analysis of both the literature and hexapod tubular data, though, reduces the S_e performance as reflected in the data touching the lower and upper bound of the literature data scatter band (Fig. 13a). The lifetime standard deviation σ_N, a performance parameter, increased from 0.27 [28] to 0.29, obtained for $\Phi = \{\sigma_N\}$. Regression of the hexapod data only provides $\sigma_{N,I} \sim 0.38$; quite worse. Note that the high-cycle fatigue hexapod data ($N > 5 \cdot 10^6$) is not assessed since no literature data is available for reference purposes. The reference weld quality literature data (Section 2.2) is added for convenience and illustrates the fit in the data scatter band.

Using the actual notch radius ρ (Table 4) – a geometry related quality aspect, rather than a conservative lower bound $\rho = 0$ like adopted for the literature data [27,28] affects S_e (Eq. 1) of the hexapod data just up to a minor extent, since $\{\rho^*_{I,AW}, \rho^*_{I,SR}\}$ is relatively large. The S_e performance did not change (Fig. 13a). An important observation is that the VA and CA hexapod data is not well aligned – although the data fits in the literature data scatter band – and seems a result of inaccurate strength and mechanism contributions; i.e. inaccurate intercept $\log(C_I)$ and slope m_I. The welding quality of the reference and hexapod data at materials level as reflected in the microstructure composition is not significantly different (Fig. 6), explaining why the mode and material characteristic ρ^* is reasonably assumed to be similar for both data sets. However, the slope of the imaginary regression line fitting the hexapod data (Figs. 8 and 13a) seems relatively large

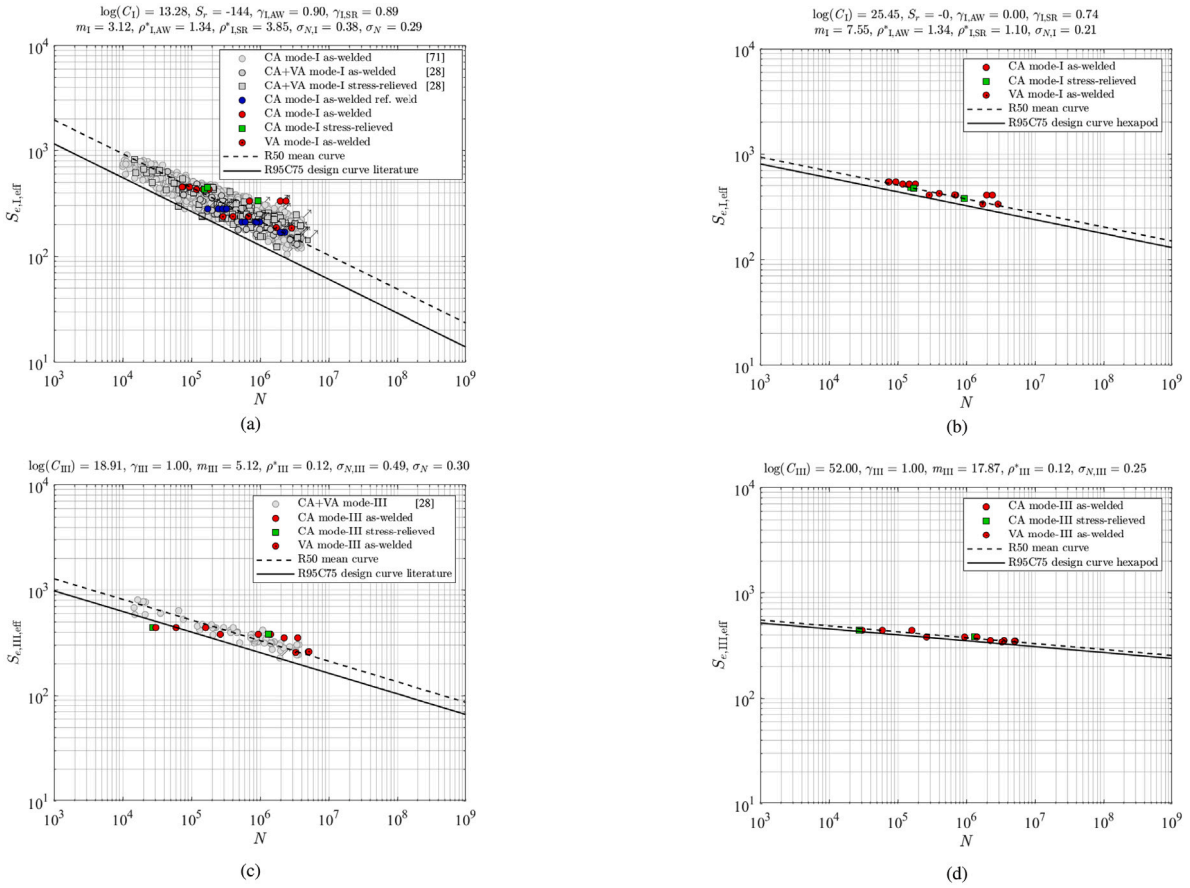

Fig. 13. Mode-I S_e resistance with enforced reference strength and mechanism parameters (a), as well as dedicated strength and mechanism parameters (b); mode-III S_e resistance with enforced (c) and dedicated (d) reference strength and mechanism parameters [65].

Table 7
Mode-{I, III} resistance S_e parameter likelihood estimates and 75% lower and upper confidence bounds.

Parameter		Reference data		Hexapod data	
$\log(C_I)$	[–]	13.28	[13.20, 13.36]	25.45	[22.59, 28.32]
m_I	[–]	3.12	[3.08, 3.15]	7.55	[6.47, 8.64]
$\rho^*_{I,AW}$	[mm]	1.34	[1.22, 1.45]	/	/
$\rho^*_{I,SR}$	[mm]	3.85	[3.56, 4.16]	/	/
$\gamma_{I,AW}$	[–]	0.90	[0.88, 0.91]	/	/
$\gamma_{I,SR}$	[–]	0.89	[0.87, 0.91]	/	/
S_r	[MPa]	−144	[−144, −143]	0	[−1, 1]
$\sigma_{N,I}$	[–]	0.21	[0.19, 0.23]	0.21	[0.16, 0.25]
$\log(C_{III})$	[–]	18.91	[18.17, 19.64]	52.00	[46.05, 57.96]
m_{III}	[–]	5.12	[4.85, 5.37]	17.87	[15.58, 20.15]
ρ^*_{III}	[mm]	0.12	[0.07, 0.21]	/	/
γ_{III}	[–]	1.00	[0.98, 1.00]	/	/
$\sigma_{N,III}$	[–]	0.21	[0.19, 0.23]	0.25	[0.20 0.31]

in comparison to the literature data, suggesting another mechanism contribution. Observing the hardness distributions (Fig. 5), smaller values are obtained for the HAZ and FZ in the hexapod specimen welds – relative to the reference ones, implying a lower cooling rate being typically responsible for reduced residual stress levels as well as decreased number and size of welding induced defects. A larger contribution of crack initiation (i.e. short crack growth) to the total lifetime as a result of residual stress not being involved and a smaller welding induced defect size seems a reasonable explanation, justifying a regression analysis of the hexapod data only in order to establish the S_e performance and dedicated most likely parameter estimates. For $\Phi = \{\log(C_I), S_r, \gamma_{I,AW}, \gamma_{I,SR}, m_I, \rho^*_{I,AW}, \rho^*_{I,SR}, \sigma_{N,I}\}$, slope $m_I \sim 7.5$, a most likely estimate in between the typical $m_I = 3$ for arc-welded joints and BM value $m_I \sim 13$ [71]. The material characteristic length estimates $\{\rho^*_{I,AW}, \rho^*_{I,SR}\}$ are similar and comparable to the literature data based values, confirming that heat treatment did not affect the hexapod data fatigue resistance as well as that based on the microstructure composition (Fig. 6) the quality of the hexapod and literature data at materials level is comparable indeed. Intercept $\log(C_I)$, reflecting the fatigue strength, naturally increased because of the $\log(C)$-m correlation for a log–log linear $S_e - N$ MCF Basquin type of relation [27]. The $S_r \sim 0$ estimate basically confirms that residual stress does not affect the fatigue strength quality of the hexapod data. Since the (mean) residual stress affects $\{\gamma_{I,AW}, \gamma_{I,SR}\}$, the most likely estimates are different from the literature data based values. As the hexapod mode-I data size is relatively small and the specimen geometry and loading conditions do not contain sufficient variability, the AW data became the reference for the SR ones. The lifetime standard deviation and performance parameter reduced to $\sigma_{N,I} = 0.21$; way below the reference data value, suggesting at first glance that an exclusive high quality hexapod data resistance curve makes sense (Fig. 13b). The fatigue strength scatter band index $T_{\sigma e,I} = 1 : 1.36$. Note that the VA hexapod data fits the CA data scatter band for the representative $\log(C_I)$ and m_I.

Because of the relatively small hexapod data size, the parameter confidence intervals are relatively large in comparison to the ones of the reference data, like illustrated for the 75% bounds (Table 7).

Comparing the mode-I R95C75 quantiles reflecting a probability of survival $p_s = 0.95$ (Fig. 13a and b), a dedicated resistance curve for the high-quality hexapod mode-I data seems to provide more accurate lifetime estimates for fatigue design purposes indeed. For general applicability the reference data curve should still be used in order to obtain conservative N values.

Principally, the (mean) residual stress quality aspect does not affect the mode-III welded joint fatigue resistance [1,28], meaning S_r is not involved nor dedicated AW and SR γ parameters are distinguished. The actual notch radius (Table 4); a geometry quality aspect, has to be incorporated since the mode-III damage accumulation is in comparison

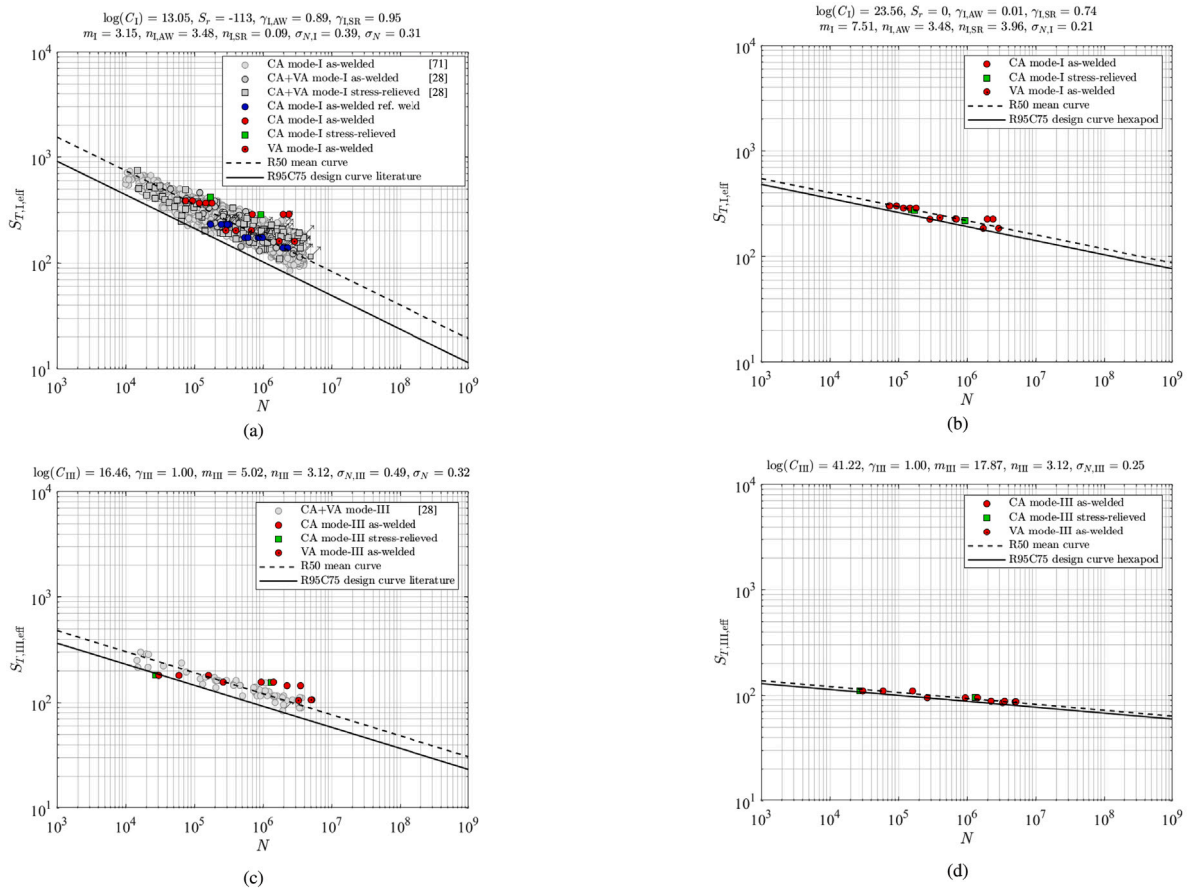

Fig. 14. Mode-I S_T resistance with enforced reference strength and mechanism parameters (a), as well as dedicated strength and mechanism parameters (b); mode-III S_T resistance with enforced (c) and dedicated (d) reference strength and mechanism parameters.

Table 8
Mode-{I, III} resistance S_T parameter likelihood estimates and 75% lower and upper confidence bounds.

Parameter		Reference data		Hexapod data	
$\log(C_I)$	[–]	13.05	[12.97, 13.13]	23.56	[21.55, 25.77]
m_I	[–]	3.15	[3.11, 3.18]	7.51	[6.58, 8.53]
$n_{I,AW}$	[–]	3.48	[3.28, 3.68]	/	/
$n_{I,SR}$	[–]	0.09	[0.01, 0.17]	/	/
$\gamma_{I,AW}$	[–]	0.89	[0.88, 0.91]	/	/
$\gamma_{I,SR}$	[–]	0.95	[0.93, 0.98]	/	/
S_r	[MPa]	−113	[−115, −110]	0	[−1, 1]
$\sigma_{N,I}$	[–]	0.22	[0.19, 0.24]	0.21	[0.16, 0.25]
$\log(C_{III})$	[–]	16.46	[15.90, 17.02]	41.42	[36.17, 46.67]
m_{III}	[–]	5.02	[4.67, 5.37]	17.87	[15.74, 20.11]
n_{III}	[–]	3.12	[1.14, 5.09]	/	/
γ_{III}	[–]	1.00	[0.98, 1.00]	/	/
$\sigma_{N,III}$	[–]	0.21	[0.18, 0.24]	0.25	[0.20, 0.30]

to mode-I a (near) surface phenomenon to an even greater extent, as reflected in $\rho^*_{III} < \rho^*_I$. Using the most likely reference parameter estimates for regression analysis of both the literature and hexapod tubular data significantly reduces the S_e performance (Fig. 13c): σ_N increased from 0.21 [1] to 0.31, obtained for $\Phi = \{\sigma_N\}$. Regression of the hexapod data only provides $\sigma_{N,III} \sim 0.30$. Because of similar microstructure composition for the reference and hexapod specimen welds (Fig. 6), ρ^*_{III} is not expected to be responsible for the reduced performance. Like for mode-I (Fig. 13a), the slope of the imaginary regression line is relatively large in comparison to the one of the literature data (Fig. 13c). Based on the comparison of the material microstructure properties for the reference and hexapod specimen welds (Section 2.3), an increased contribution of crack initiation to the total lifetime explains the change in mechanism, in slope m_{III}. Regression analysis for $\Phi = \{\log(C_{III}), \gamma_{III}, m_{III}, \sigma_{N,III}\}$ provides slope $m_{III} \sim 17.9$, a most likely estimate close to the BM value $m_{III} \sim 18$ [71]. Except a similar microstructure composition, the specimen geometry and loading conditions variability is insufficient nor different thermal conditions are involved, explaining why the reference material characteristic length is adopted: $\rho^*_{III} \sim 0.12$. Intercept $\log(C_{III})$, reflecting the fatigue strength, naturally increased because of the $\log(C) - m$ correlation. Mean (residual) stress does not affect the fatigue strength quality of the hexapod data, as reflected in the $\gamma_{III} \sim 1$ estimate. The performance parameter reduced to $\sigma_{N,III} = 0.25$; an improvement in comparison to the $\sigma_{N,III} \sim 0.30$ estimate as obtained for using the reference parameter values (Fig. 13d). The fatigue strength scatter band index $T_{\sigma S_e,III} = 1 : 1.14$.

Like for mode-I, the parameter confidence intervals are relatively large in comparison to the ones of the reference data, as illustrated for the 75% bounds (Table 7). Comparing the mode-III R95C75 quantiles (Fig. 13c and d), a dedicated resistance curve for the high-quality hexapod mode-III data seems to provide more accurate lifetime estimates. Non-conservative N values at the MCF region lower bound can even be obtained when applying the reference data curve.

For the total stress S_T as fatigue strength parameter (Eq. 2), uniaxial mode-I MCF reference resistance for planar and tubular geometries in steel (maritime) structures has already been established for CA and VA literature data as well [29]. To fit the MCF hexapod data into the $S_T - N$ literature data scatter band, S_r will be applied for both the AW and SR thermal conditions, since no significant residual stress is involved. At the same time, S_r affects the notch and crack tip elastoplastic behaviour, explaining why $n_{I,AW}$ has been used for all the hexapod data. Adopting the most likely reference parameter estimates,

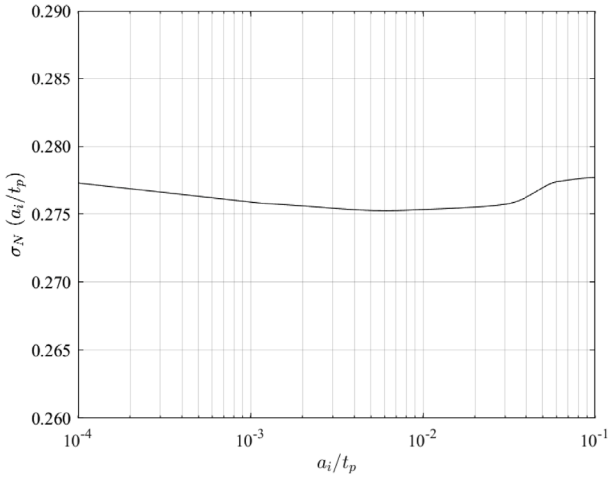

Fig. 15. Most likely σ_N for a range of $a_i/t_p|_{a_i/t_p=1}$.

regression analysis of both the literature and hexapod tubular data for $\Phi = \{\sigma_N\}$ reduces the S_T performance as reflected in the hexapod data touching the bounds of the literature data scatter band (Fig. 14a), like for S_e (Fig. 13a): σ_N increased from 0.30 [29] to 0.31. Regression of the MCF hexapod data only provides $\sigma_{N,I} \sim 0.39$; quite worse. The reference quality literature data (Section 2.2) is added for convenience and illustrates the fit in the literature data scatter band. Using the actual notch radius ρ (Table 4) – a geometry related quality aspect – affects the notch factor Y_n (Eq. 10 and 11) for $(a/t_p) \to 0$, but the square root singularity for small cracks close to the notch surface (radius) controls the crack growth integral I_N (Eq. 10 and 11); i.e. S_T, meaning the performance hardly changed (Fig. 14a). Like observed for S_e (Fig. 13a), the damage mechanism seems responsible for the different slope of the imaginary regression line fitting the hexapod data in comparison to the one of the literature data. The material microstructure properties (Section 2.3) principally support the hypothesis of a larger contribution of crack initiation to the total lifetime because of no residual stress and a decreased number and size of welding induced defects. Regression analysis of all the hexapod data only; i.e. uniaxial and multiaxial, for $\Phi = \{\log(C_I), m_I, \sigma_{N,I}\}$ and varying defect size shows that with respect to the lifetime standard deviation $\sigma_{N,I}$ still $(a_i/t_p) \sim 6 \cdot 10^{-3}$ is the most likely estimate (Fig. 15). An import note, however, is that the parameters affecting (a_i/t_p) the most; in particular the mean stress and elastoplasticity coefficients $\{\gamma, n\}$, are the same as for the literature data, meaning proof of a smaller welding induced defect size would require additional test data, obtained for different geometry – in particular wall thickness t_p – and different R levels. Slope $m_I \sim 7.5$ is more than double the typical $m_I = 3$ value for arc-welded joints, confirming the change in mechanism. The elastoplasticity coefficients estimates $\{n_{I,AW}, n_{I,SR}\}$ are similar and comparable to the literature data based values, confirming that S_r did not affect the hexapod data fatigue resistance indeed as well as that notch and crack tip elastoplasticity affected short crack growth behaviour for the AW and SR data is about the same. Explanations for $\log(C_I)$, S_r and $\{\gamma_{I,AW}, \gamma_{I,SR}\}$ as provided for S_e still hold for S_T (Fig. 14b): respectively a natural increase because of the $\log(C) - m$ correlation, a confirmation that (mean) residual stress does not affect the hexapod data fatigue strength and the AW data being reference for the SR ones since the data size is relatively small and sufficient specimen geometry and loading condition variability is lacking. The lifetime standard deviation reduced to $\sigma_{N,I} = 0.21$; way below the reference data value, suggesting an exclusive hexapod data resistance curve makes sense (Fig. 14b). The fatigue strength scatter band index $T_{\sigma S_{T,I}} = 1 : 1.36$. Dedicated $\log(C_I)$ and m_I parameters ensure the VA hexapod data fits the CA data scatter band. Note that the S_e and S_T performance is similar, like observed before [29].

The parameter confidence intervals are relatively large in comparison to the ones of the reference data because of the relatively small hexapod data size, like illustrated for the 75% bounds (Table 8). The mode-I R95C75 quantiles reflect a probability of survival $p_s = 0.95$ (Fig. 14a and b) and suggest that a dedicated resistance curve for the high-quality hexapod mode-I data provides more accurate lifetime estimates for fatigue design purposes. Applying the reference data curve for general purposes provides conservative N values.

Since the residual stress hardly affects the mode-III welded joint fatigue resistance [1,28], S_r is not involved nor dedicated AW and SR γ parameters are distinguished. The actual notch radius (Table 4) is incorporated since mode-III damage accumulation is a (near) surface phenomenon up to a large extent. Using the most likely reference parameter estimates for regression analysis of both the literature and hexapod tubular data significantly reduces the S_T performance (Fig. 14c): σ_N increased from 0.21 [29] to 0.32, obtained for $\Phi = \{\sigma_N\}$. Regression of the hexapod data only provides $\sigma_{N,III} \sim 0.49$. Since the microstructure composition for the reference and hexapod specimen welds are similar (Fig. 6) and at the same time S_r – affecting the notch and crack tip elastoplastic behaviour – does not significantly influence the mode-III fatigue resistance, n_{III} is not expected to be responsible for the reduced performance. As for mode-I (Fig. 14a), the slope of the imaginary regression line is relatively large in comparison to the one of the literature data (Fig. 14c) and likely a result of an increased contribution of crack initiation to the total lifetime, as reflected in the material microstructure properties for the reference and hexapod specimen welds (Section 2.3). Regression analysis for $\Phi = \{\log(C_{III}), \gamma_{III}, m_{III}, \sigma_{N,III}\}$ provides slope $m_{III} \sim 17.9$, a most likely estimate close to the BM value $m_{III} \sim 18$ [71]. Except a similar microstructure composition, the specimen geometry and loading conditions variability is insufficient nor thermal conditions are involved, explaining why the reference elastoplasticity coefficient is adopted: $n_{III} \sim 3.12$. Intercept $\log(C_{III})$, reflecting the fatigue strength, naturally increased because of the $\log(C) - m$ correlation. Mean (residual) stress does not affect the fatigue strength quality of the hexapod data, as reflected in the $\gamma_{III} \sim 1$ estimate. The lifetime standard deviation reduced to $\sigma_{N,III} = 0.25$; an improvement in comparison to the $\sigma_{N,III} \sim 0.32$ estimate as obtained for using the reference parameter values (Fig. 14d). The fatigue strength scatter band index $T_{\sigma S_{T,III}} = 1 : 1.14$.

Like for mode-I, the parameter confidence intervals are relatively large in comparison to the ones of the reference data, as illustrated for the 75% bounds (Table 8). Comparing the mode-III R95C75 quantiles (Fig. 14c and d), a dedicated resistance curve for the high-quality hexapod mode-III data seems to provide more accurate lifetime estimates. The literature data curve may provide non-conservative N estimates.

Comparing the uniaxial mode-{I, III} MCF resistance (Fig. 16), σ_N illustrates a similar performance for S_e and S_T; respectively an intact and cracked geometry parameter. Linear damage accumulation up to $D = 1$ shows VA data fitting the CA data scatter band. The different strength and mechanism as reflected in $\{\log(C), \gamma\}$, as well as $\{m, \rho^*\}$ or $\{m, n\}$ for S_e and S_T respectively, suggesting a lifetime dependent shear strength coefficient $\beta(N)$ rather than a constant one β is required for multiaxial fatigue assessment. Note that the strength and mechanism contributions for the high-quality hexapod data is quite different from the reference-quality literature data [28,29], affecting $\beta(N)$.

3.4. Multiaxial resistance

Adopting the von Mises criterion S_e (Eq. 1), the reference data uniaxial mode-{I, III} strength and mechanism parameters $\{\gamma_{I,AW}, \rho^*_{I,AW}, \rho^*_{III}\}$ as well as the optimum 1st order non-proportionality coefficients (Eq. 4) C_{np} and c_m [28], the multiaxial hexapod data fits the data scatter band (Fig. 17a). Conservative design lifetime estimates can be obtained, but the data is quite scattered as reflected in $\sigma_N = 0.38$; relative large with respect to $\sigma_N = 0.29$ of the reference data. For the uniaxial mode-{I, III} strength and mechanism estimates of the hexapod data (Fig. 16a), the optimum non-proportionality measure

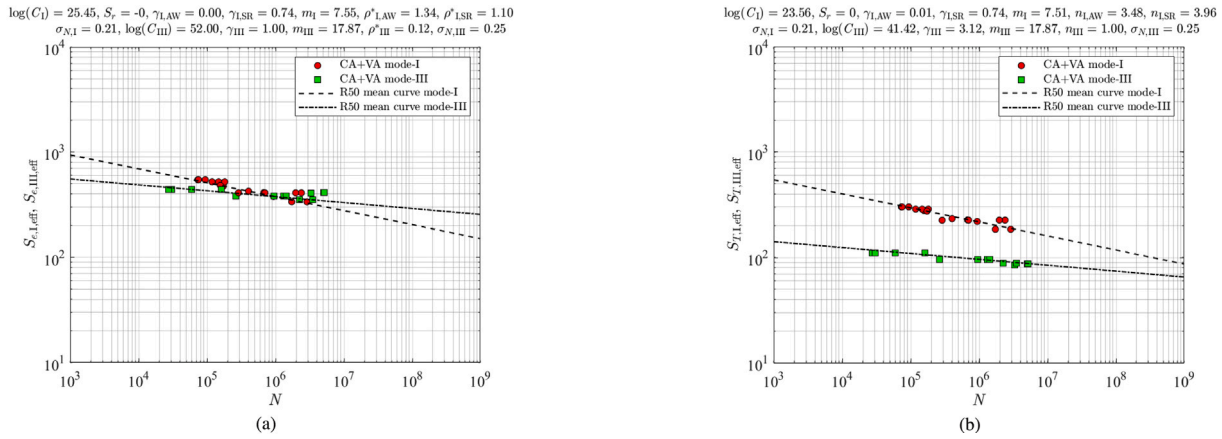

Fig. 16. Uniaxial mode-{I, III} hexapod data fatigue resistance for S_e (a) and S_T (b).

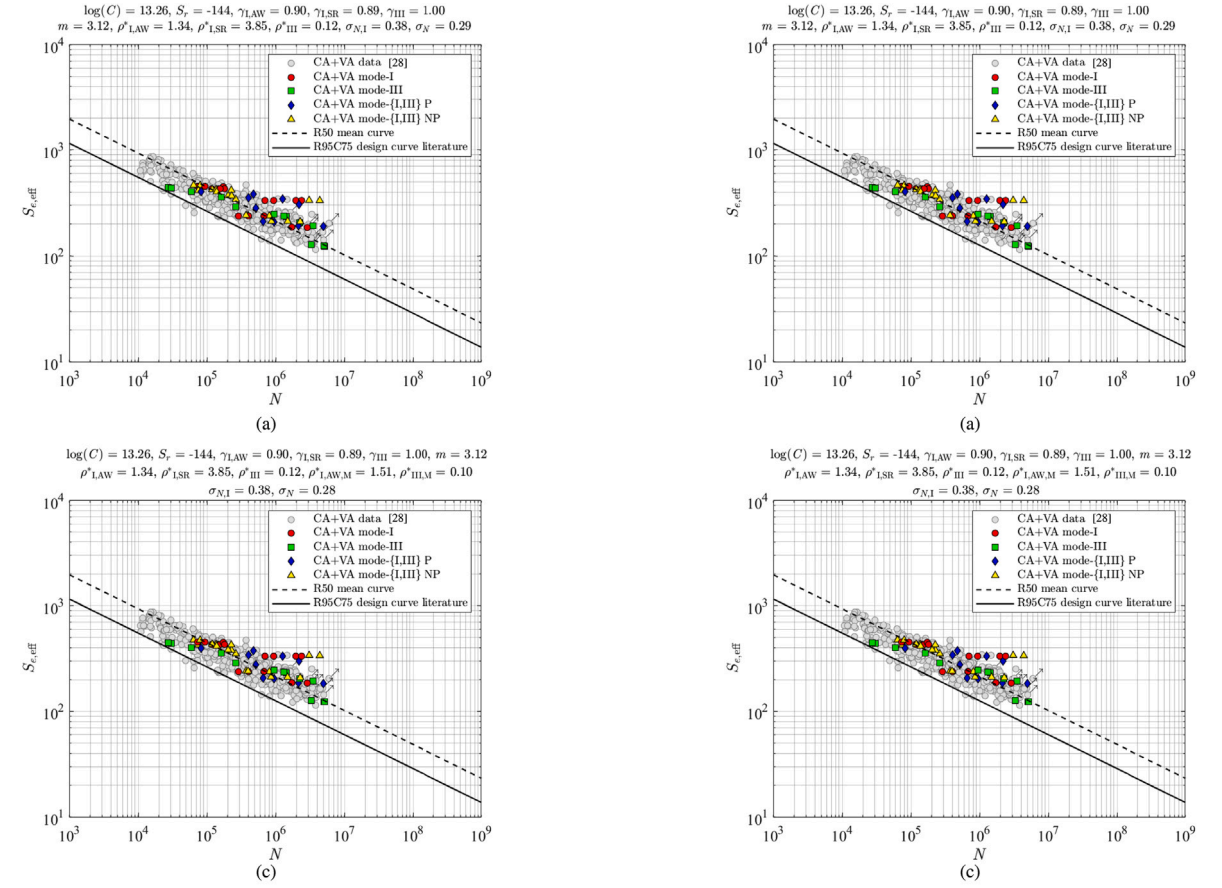

Fig. 17. Effective notch stress based hexapod multiaxial fatigue resistance for uniaxial ρ^* values and reference parameters; $c_m = 0.40$ (a), uniaxial ρ^* values and dedicated parameters; $c_m = 0.45$ (b), multiaxial ρ^* values and reference parameters; $c_m = 0.50$ (c), multiaxial ρ^* values and dedicated parameters; $c_m = 0.45$ (d).

turned out to be still 1st order. The possibility of c_m being a material characteristic holds [28] since the value hardly changed (Fig. 17b) – recalling the similar material microstructure for the hexapod and reference specimen welds (Fig. 6), but proof is not conclusive. The lifetime standard deviation, however, reduced to $\sigma_N = 0.29$, equal to the reference data value and implying a relatively narrow scatter band (Fig. 17b). For the reference data, mode-{I, III} coupling is introduced in order to explain the multiaxial fatigue resistance characteristics [29], reflected in the introduced mechanism parameters $\{\rho^*_{I,AW,M}, \rho^*_{III,M}\}$. Dedicated hexapod data values are obtained as well, but are quite close to the reference ones. The scatter of the individual multiaxial data groups, P and NP, did change, but the similar σ_N may suggest any possible influence of mode-{I, III} coupling might be limited. However, the hexapod data geometry and loading variations are too limited to provide a conclusive answer. Only a small S_e improvement is gained (Fig. 17c and d), knowing that the concept of stress averaging implies a relatively small ρ^* sensitivity anyway. The lifetime standard deviation reduced to $\sigma_N = 0.28$ and relatively accurate lifetime estimates can be obtained.

The IIW design guidelines [72] have been used for comparison purposes, in order to illustrate the S_e performance. Applying a reference notch radius ρ_r of 1 [mm] rather than averaging the notch stress distribution over a material characteristic length ρ^* (Section 3.1) to obtain S_e, notch factors are established for all loading components with

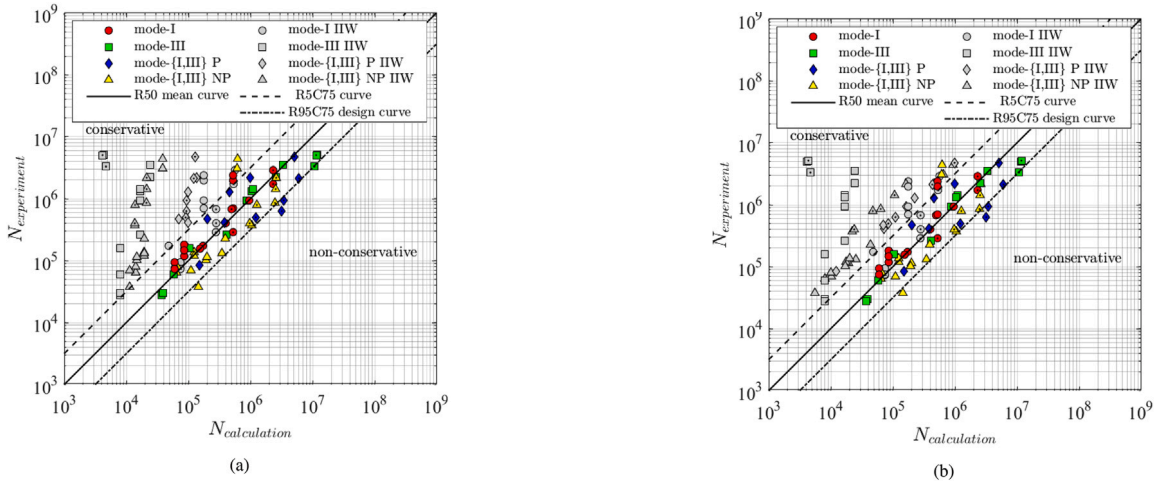

Fig. 18. Fatigue lifetime ratio plot comparing the performance of the IIW guidelines for a lifetime dependent (a) and FAT class (b) defined resistance formulation, as well as the proposed S_e parameter with the mode-specific hexapod specimen weld strength and mechanism contributions. The · at a data point centre indicates a VA test result.

respect to the nominal stress reference plane (Fig. 2): $K_f = 2.12$ for a normal force F_n, $K_f = 2.11$ for a bending moment M_b and $K_f = 1.52$ for a torsion moment M_t. The interaction equation $\{S_{e,I}/S_{e,I,r}(N)\}^2 + \{S_{e,III}/S_{e,III,r}(N)\}^2 \leq CV$ involving the mode-I and mode-III design curve formulations $S_{e,I,r}(N)$ and $S_{e,III,r}(N)$ – respectively based on the FAT classes 225 and 160, slope $m = 3$ and 5 – is solved for the design life time estimate $N = N_{calculation}$ [e.g. 73]. Comparison value CV is 1.0 for P and 0.5 for NP multiaxiality. For VA loading conditions, $\{S_{e,I}, S_{e,III}\}$ turn into equivalent ones $\{S_{e,I,eq}(D), S_{e,III,eq}(D)\}$, obtained using rain flow counting of the individual mode-I and mode-III time signals of the hexapod specimen welds and a linear damage accumulation model. Damage D is 0.5 for P and 0.2 for NP amplitude variability. However, rather than incorporating the actual mode-I and mode-III contributions defining the life time dependent resistance based ratio of S_I and S_{III}, the fixed FAT class based ratio can be adopted as well [e.g. 74], involving $S_{e,I,r}(N = 2 \cdot 10^6)$ and $S_{e,III,r}(N = 2 \cdot 10^6)$. The choice seems to depend on the interpretation of the guidelines. Solving the interaction equation for CV first, $N_{calculation} = (CV/D) \cdot N_{experimental}$ can be obtained afterwards. From design perspective, at least conservative lifetime estimates are obtained for both the lifetime dependent and the FAT class based resistance formulation (Fig. 18). However, $N_{calculation}$ is not that accurate and the scatter band is quite large in comparison to the results obtained using a notch stress averaged S_e parameter with the actual – i.e. different – mode-specific hexapod specimen weld strength and mechanism contributions affecting the resistance curve intercept and slope (Figs. 17d and 18).

Assessment of the hexapod data using the total stress S_T (Eq. 2) provides similar results. For the reference quality literature data parameters a fit in the scatter band is obtained (Fig. 19a), although the high-quality hexapod data is clearly at the upper bound. Dedicated hexapod data parameters including the non-proportionality coefficients $\{C_{np}, c_m\}$ provide a much better fit (Fig. 19b): σ_N reduced from 0.38 to 0.24, even smaller than the S_e value (Fig. 17b). The optimum material characteristic c_m reduced a bit, but is still similar to the reference data value. Although mode-{I, III} coupling improved the S_T reference data formulation up to some extent [29], for the hexapod data no obvious differences are observed (Fig. 19c and d). The elastoplasticity coefficients $\{n_{I,AW,M}, n_{III,M}\}$ are similar to the uniaxial values, explaining the unaffected σ_N. Like for S_e, the scatter of the individual multiaxial data groups did change, but geometry and loading limitations prevent for conclusive evidence of coupling effects. In general, the small crack size singularity dominates the crack growth integral (Eqs. 10 and 11) and is quite sensitive to the involved elastoplasticity coefficient n – in contrast to the ρ^* sensitivity for S_e. Accurate design lifetime estimates can be obtained.

4. Conclusions and outlook

The custom-built TU Delft hexapod for mechanical testing purposes, allowing for relatively large loads and smaller motions at all six individually controlled DoF's, turned out to be an excellent test rig for multiaxial CA and VA fatigue testing.

Tubular arc-welded double-sided T-joints are manufactured for demanding offshore applications. The acceptance criteria for visual and magnetic particle inspection, respectively class B and level 2X, proves high quality in terms of strength, geometry, material and mechanism aspects, as respectively reflected in a negligible residual stress, a relatively large notch radius, a homogeneous microstructure in the WM and HAZ and a gradual hardness distribution at a relatively low level. Taking all aspects into account fits the (mixed) mode-{I, III} hexapod test data in the reference quality fatigue literature data scatter band for advanced multiaxial criteria: the effective notch stress S_e and the total stress S_T; an intact and cracked geometry parameter. Support for the residual $S_r = 0$ is observed in the material microstructure properties as well as the AW and SR fatigue test data; in particular the mode-I resistance (contribution) is affected for both S_e and S_T. Mode-III resistance is hardly (mean) residual stress sensitive. The real notch radius ρ slightly affects the mode-I fatigue resistance for S_e and S_T, respectively because of the relatively large ρ_I^* and the square root singularity for small cracks close to the notch surface (radius) being governing. However, for mode-III ρ has to be incorporated considering S_e, because of the relatively small ρ_{III}^* reflecting a near surface phenomenon. For S_T, on the other hand, ρ is less important for the same reason as mentioned for mode-I. Similar material microstructure compositions for the (literature) reference and hexapod specimen weld suggest that the fatigue mechanism parameters ρ^* and n for respectively S_e and S_T are not very different, as confirmed in the hexapod data likelihood regression results. Although the material microstructure properties support a smaller welding induced defect size (a_i/t_p) for the high-quality hexapod data, the variation in geometry and loading conditions – mean stress in particular – is insufficient and conclusive proof cannot be provided, since the literature data based strength and mechanism parameter estimates $\{\gamma, n\}$ rather than dedicated ones had to be adopted for S_T; the same ones as used to obtain the most likely (a_i/t_p) for the reference quality literature fatigue test data.

Since the multiaxial hexapod fatigue test data fits the reference data scatter band, conservative lifetime estimates can be obtained adopting S_e and S_T with the reference data strength and mechanism parameters. However, dedicated hexapod data parameters significantly improve the accuracy, distinguishing the high-quality welded joints from the reference ones. Like observed for the reference data, the performance

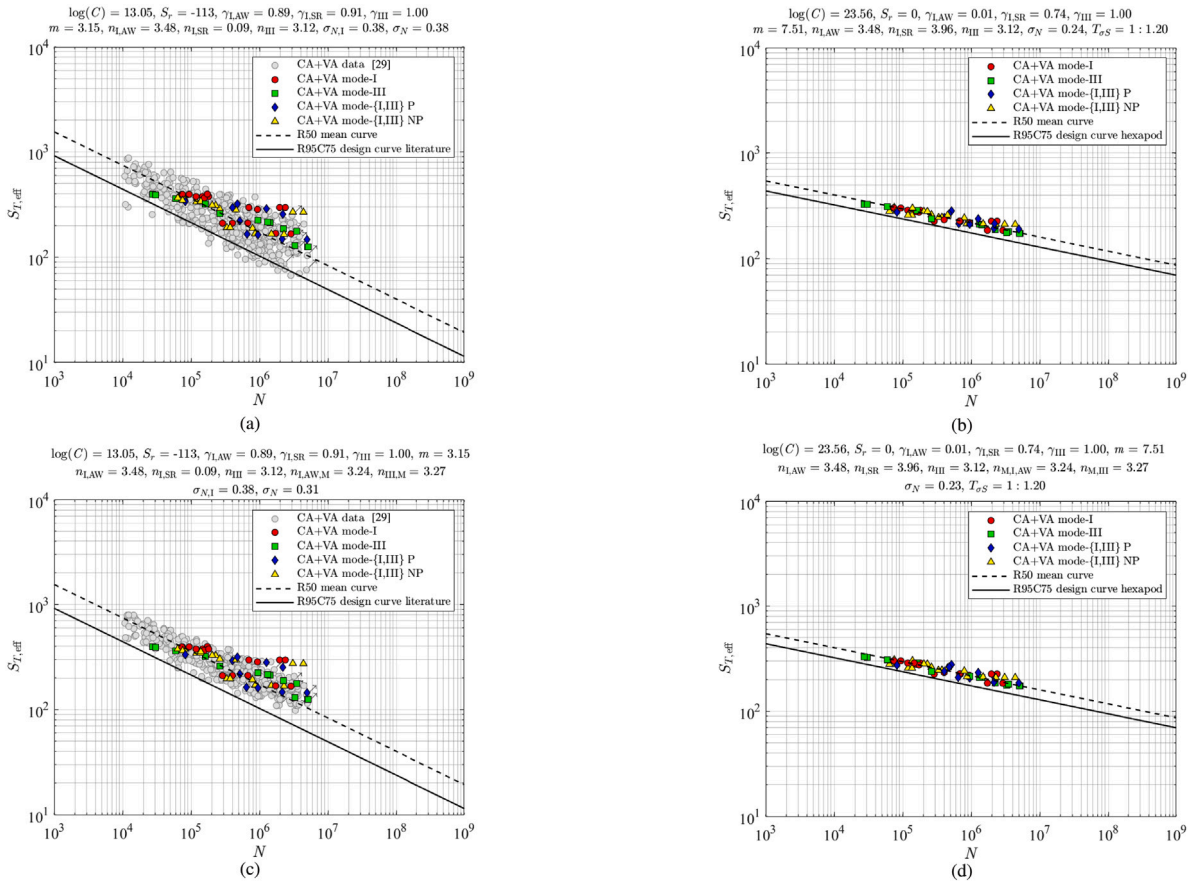

Fig. 19. Total stress based hexapod multiaxial fatigue resistance for uniaxial n values and reference parameters; $c_m = 0.45$ (a), uniaxial n values and dedicated parameters; $c_m = 0.40$ (b), multiaxial n values and reference parameters; $c_m = 0.60$ (c), multiaxial n values and dedicated parameters; $c_m = 0.45$ (d).

of S_T is better than of S_e, as reflected in σ_N. Whereas the S_e related ρ^* equivalent for S_T is the final crack size (a_f/t_p), S_T has one more mechanism parameter in terms of the elastoplasticity coefficient n to model the fatigue (crack growth) behaviour, providing more accurate lifetime estimates. Mode-{I, III} coupling improves the individual multiaxial data set performance with respect to (non-) proportionality for S_e and S_T, but hardly affects the overall performance defining the resistance curve. For particular multiaxial loading and response conditions, coupling can be important, although conclusive proof for the hexapod data cannot be provided because of limited geometry and loading variations.

High-quality welded joint fatigue resistance is predominantly reflected in the larger resistance curve intercept $\log(C)$ and slope m; a strength and a mechanism parameter, implying a larger initiation (i.e. short crack growth) contribution to the total lifetime. Still adopting the reference quality related resistance curve $\{\log(C), m\}$ for high-quality hexapod data means, however, for VA loading and response conditions that damage equivalence is lost. Despite the smaller parameter confidence for the high-quality welded joint fatigue resistance because of the smaller hexapod data size, the design life estimates are more accurate in comparison to the conservative reference quality literature data based estimates. In order to improve the basis for a high quality hexapod data fatigue resistance curve, more tests are required with different geometry and mean (residual) stress conditions to obtain dedicated strength and mechanism parameters, i.e. $\{\gamma, \rho^*\}$ for S_e and $\{\gamma, n\}$ as well as (a_i/t_p) for S_T.

For general fatigue assessment applications, a reference quality based resistance curve is recommended from design perspective. If high-quality resistance can be guaranteed, a dedicated curve can be used. For the most accurate lifetime estimates S_T is preferred as fatigue strength parameter. However, balancing computational efforts, parameter complexity and accuracy, S_e can be adopted as well.

CRediT authorship contribution statement

Gabriele Bufalari: Writing – original draft, Visualization, Validation, Software, Methodology, Investigation, Formal analysis, Data curation, Conceptualization. **Niels Troost:** Writing – review & editing, Investigation, Formal analysis. **Henk den Besten:** Writing – review & editing, Supervision, Resources, Methodology, Conceptualization. **Miroslaw Lech Kaminski:** Writing – review & editing, Supervision, Project administration, Funding acquisition, Conceptualization.

Declaration of competing interest

The authors declare that they have no known competing financial interests or personal relationships that could have appeared to influence the work reported in this paper.

Acknowledgment

The authors are grateful for the support and funding of the 4D-Fatigue project provided by the Dutch Research Council (NWO) as part of the programme “Maritime” (file number 13270), as well as the industry partners Allseas, Bluewater Energy Services, Bureau Veritas, C-Job, Damen Shipyards, DNV, Dutch Ministry of Defence, Femto Engineering, Huisman Equipment, Jumbo Maritime, Lloyd’s Register, MARIN, OCAS, Office of Naval Research, Royal IHC, Royal Roos, SBM Offshore, Shell, Total Energies and Vallen Systeme.

Appendix. Hexapod fatigue test data

Table A.9
Constant amplitude loading results.

Load case	$\Delta\sigma_n$ [a] [MPa]	$\Delta\tau_n$ [a] [MPa]	N [–]	R_I [–]	R_{III} [–]	ph.shift [°]	freq.ratio $\sigma:\tau$ [–]	th. cond.
Normal force	175		$5.18 \cdot 10^6$	0.1				AW
F_n	175		$1.06 \cdot 10^7$	0.1				AW
Bending moment	320		$7.32 \cdot 10^4$	0.1				AW
M_b	320		$7.48 \cdot 10^4$	0.1				AW
	320		$9.38 \cdot 10^4$	0.1				AW
	305		$1.18 \cdot 10^5$	0.1				AW
	305		$1.47 \cdot 10^5$	0.1				AW
	305		$1.81 \cdot 10^5$	0.1				AW
	240		$6.98 \cdot 10^5$	0.1				AW
	240		$1.97 \cdot 10^6$	0.1				AW
	240		$2.39 \cdot 10^6$	0.1				AW
	305		$8.19 \cdot 10^6$	−1				AW
	305		$1.56 \cdot 10^5$	0.1				SR
	240		$9.36 \cdot 10^5$	0.1				SR
	370		$1.73 \cdot 10^5$	−1				SR
Torsion moment		318	$3.03 \cdot 10^4$		−1			AW
M_t		318	$5.97 \cdot 10^4$		−1			AW
		318	$1.61 \cdot 10^5$		−1			AW
		274	$2.63 \cdot 10^5$		−1			AW
		274	$9.41 \cdot 10^5$		−1			AW
		274	$1.42 \cdot 10^6$		−1			AW
		254	$3.53 \cdot 10^6$		−1			AW
		254	$2.24 \cdot 10^6$		−1			AW
		242	[b] $1.19 \cdot 10^7$		−1			AW
		231	[b] $1.71 \cdot 10^7$		−1			AW
		318	$2.75 \cdot 10^4$		−1			SR
		274	$1.31 \cdot 10^6$		−1			SR
M_b and M_t induced multiaxial in-phase	240	139	$8.32 \cdot 10^4$	0.1	0.1	0	1	AW
	240	139	$4.73 \cdot 10^5$	0.1	0.1	0	1	AW
	220	127	$4.07 \cdot 10^5$	0.1	0.1	0	1	AW
	220	127	$1.28 \cdot 10^6$	0.1	0.1	0	1	AW
	200	115	$2.17 \cdot 10^6$	0.1	0.1	0	1	AW
	200	115	$9.11 \cdot 10^6$	0.1	0.1	0	1	AW
	170	98	[b] $2.00 \cdot 10^7$	0.1	0.1	0	1	AW
M_b and M_t induced multiaxial 90° out-of-phase	260	150	$6.40 \cdot 10^4$	0.1	0.1	90	1	AW
	260	150	$7.99 \cdot 10^4$	0.1	0.1	90	1	AW
	240	139	$1.19 \cdot 10^5$	0.1	0.1	90	1	AW
	240	139	$1.37 \cdot 10^5$	0.1	0.1	90	1	AW
	200	115	$3.07 \cdot 10^6$	0.1	0.1	90	1	AW
	200	115	$4.38 \cdot 10^6$	0.1	0.1	90	1	AW
	170	98	[b] $2.00 \cdot 10^7$	0.1	0.1	90	1	AW
M_b and M_t induced multiaxial 1 : 3 asynchronous[c]	240	139	$3.76 \cdot 10^4$	0.1	0.1	0	3	AW
	240	139	$6.94 \cdot 10^4$	0.1	0.1	0	3	AW
	225	130	$1.02 \cdot 10^5$	0.1	0.1	0	3	AW
	225	130	$1.14 \cdot 10^5$	0.1	0.1	0	3	AW
	210	121	$1.32 \cdot 10^5$	0.1	0.1	0	3	AW
	210	121	$2.26 \cdot 10^5$	0.1	0.1	0	3	AW
	190	110	[b] $7.49 \cdot 10^6$	0.1	0.1	0	3	AW
	170	98	[b] $7.83 \cdot 10^6$	0.1	0.1	0	3	AW

[a] $\Delta\sigma_n = \Delta F_n / A_n$ or $\Delta\sigma_n = \Delta M_b / Z_b$, $\Delta\tau_n = \Delta M_t / Z_t$ (Fig. 2a); min and max $\{F_n, M_b, M_t\}$ values can be obtained using $\{R_I, R_{III}\}$.
[b] runout
[c] N corresponds to $\Delta\sigma_n$ cycles

Table A.10
Variable amplitude loading results.

Load case	$\Delta\sigma_{n,max}$ [a] [MPa]	$\Delta\tau_{n,max}$ [a] [MPa]	N [–]	R_I [–]	R_{III} [–]	ph.shift [°]	freq. ratio $\sigma : \tau$ [–]	th. cond.
Bending moment M_b	320		$2.88 \cdot 10^5$	0.1				AW
	320		$4.02 \cdot 10^5$	0.1				AW
	320		$6.77 \cdot 10^5$	0.1				AW
	260		$1.72 \cdot 10^6$	0.1				AW
	260		$2.88 \cdot 10^6$	0.1				AW
	260		$5.89 \cdot 10^6$	0.1				AW
	260		[b] $1.00 \cdot 10^7$	0.1				AW
Torsion moment M_t		570	$5.02 \cdot 10^6$		–1			AW
		570	$5.15 \cdot 10^6$		–1			AW
		570	$3.29 \cdot 10^6$		–1			AW
M_b and M_t induced multiaxial in-phase	267	154	$4.97 \cdot 10^5$	0.1	0.1	0	1	AW
	267	154	$6.31 \cdot 10^5$	0.1	0.1	0	1	AW
	267	154	$9.36 \cdot 10^5$	0.1	0.1	0	1	AW
	242	140	$2.12 \cdot 10^6$	0.1	0.1	0	1	AW
	242	140	$4.75 \cdot 10^6$	0.1	0.1	0	1	AW
	235	136	[b] $1.00 \cdot 10^7$	0.1	0.1	0	1	AW
	235	136	[b] $1.00 \cdot 10^7$	0.1	0.1	0	1	AW
M_b and M_t induced multiaxial 90° out-of-phase	290	167	$3.70 \cdot 10^5$	0.1	0.1	90	1	AW
	290	167	$4.00 \cdot 10^5$	0.1	0.1	90	1	AW
	290	167	$7.93 \cdot 10^5$	0.1	0.1	90	1	AW
	267	154	$8.55 \cdot 10^5$	0.1	0.1	90	1	AW
	267	154	$1.43 \cdot 10^6$	0.1	0.1	90	1	AW
	267	154	$2.17 \cdot 10^6$	0.1	0.1	90	1	AW

[a] $\Delta\sigma_{n,max} = \Delta F_n / A_n$ or $\Delta\sigma_{n,max} = \Delta M_b / Z_b$, $\Delta\tau_{n,max} = \Delta M_t / Z_t$ (Fig. 2a); min and max $\{F_n, M_b, M_t\}$ values can be obtained using $\{R_I, R_{III}\}$.
[b] runout.

Data availability

The references for the literature fatigue test data are provided and the hexapod data is available in Appendix A.

References

[1] Bufalari G, den Besten H, Kaminski ML. Mode-lll fatigue of welded joints in steel maritime structures: Weld notch shear stress distributions and effective notch stress based resistance. Int J Fatigue 2022;107210. http://dx.doi.org/10.1016/J.IJFATIGUE.2022.107210.

[2] Hieu TV, Hong NT. Mechanical engineering excellence: Design and optimization of two-dimensional fatigue testing machines. Q J Emerg Technol Innov 2024;9:1–14.

[3] Anes V, Reis L, Li B, Fonte M, Freitas MD. New approach for analysis of complex multiaxial loading paths. Int J Fatigue 2014;62:21–33. http://dx.doi.org/10.1016/j.ijfatigue.2013.05.004.

[4] Benasciutti D, Sherratt F, Cristofori A. Basic principles of spectral multi-axial fatigue analysis. Procedia Eng 2015;101:34–42. http://dx.doi.org/10.1016/j.proeng.2015.02.006.

[5] Sonsino CM. Multiaxial fatigue assessment of welded joints - recommendations for design codes. Int J Fatigue 2009;31:173–87. http://dx.doi.org/10.1016/j.ijfatigue.2008.06.001.

[6] Susmel L. A simple and efficient numerical algorithm to determine the orientation of the critical plane in multiaxial fatigue problems. Int J Fatigue 2010;32:1875–83. http://dx.doi.org/10.1016/J.IJFATIGUE.2010.05.004.

[7] Meneghetti G, Campagnolo A, Babini V, Riboli M, Spagnoli A. Multiaxial fatigue assessment of welded steel details according to the peak stress method: Industrial case studies. Int J Fatigue 2019;125:362–80. http://dx.doi.org/10.1016/j.ijfatigue.2019.04.014.

[8] Kim I-T, Yamada K. Fatigue behaviour of fillet welded joints inclined to a uniaxial cyclic load. In: IIW document XIII-2021-04. 2004.

[9] Maddox SJ. Fatigue assessment of welds not oriented either normal or parallel to the direction of loading. In: IIW document J WG XIII/ XV- 218- 10. 2010.

[10] Dahle T, Olsson KE, Samuelsson J. Fatigue design optimisation of welded box beams subjected to combined bending and torsion. Eur Struct Integr Soc 1999;23:103–16. http://dx.doi.org/10.1016/S1566-1369(99)80034-X.

[11] Quaresimin M, Susmel L. Multiaxial fatigue behaviour of composite laminates. Key Eng Mater 2001;221–222:71–80. http://dx.doi.org/10.4028/www.scientific.net/kem.221-222.71.

[12] Costa P, Nwawe R, Soares H, Reis L, Freitas M, Chen Y, Montalvão D. Review of multiaxial testing for very high cycle fatigue: From 'conventional' to ultrasonic machines. Machines 2020;8(2):25. http://dx.doi.org/10.3390/machines8020025.

[13] Costa P, Soares H, Reis L, Freitas M. Ultrasonic fatigue testing under multiaxial loading on a railway steel. Int J Fatigue 2020;136:11. http://dx.doi.org/10.1016/j.ijfatigue.2020.105581.

[14] Kamaya M. Development of disc bending fatigue test technique for equi-biaxial loading. Int J Fatigue 2016;82:561–71. http://dx.doi.org/10.1016/j.ijfatigue.2015.09.012.

[15] Almamoori MK, Alizadeh Y, Abolghasemzadeh M. A review of multi-axial fatigue tests. IOP Conf Ser: Mater Sci Eng 2021;1094(1):012058. http://dx.doi.org/10.1088/1757-899x/1094/1/012058.

[16] Morishita M, Gotoh K, Anai Y, Tsumura S, Niwa T. Fatigue surface crack growth behavior in flat plate and out-of-plane gusset-welded joints under biaxial cyclic loads with different phases. J Mar Sci Technol 2020;26(3):655–72. http://dx.doi.org/10.1007/s00773-020-00762-1.

[17] Chen J, Zhang J. Optimal boundary shape of the center-reduced cruciform specimen for the in-plane biaxial test. In: Advances in machinery, materials science and engineering application. IOS Press; 2022, http://dx.doi.org/10.3233/atde220463.

[18] Gryguc A, Behravesh S, Jahed H, Wells M, Macek W, Williams B. The multiaxial load proportionality effect on the fracture surface topography of forged magnesium alloys. In: 13th international conference on multiaxial fatigue and fracture. ICMFF13, 2022.

[19] Seo J-W, Hur H-M, Jun H-K, Kwon S-J, Lee D-H. Fatigue design evaluation of railway bogie with full-scale fatigue test. Adv Mater Sci Eng 2017;2017:1–11. http://dx.doi.org/10.1155/2017/5656497.

[20] Kvistedal Y, Nielsen P. Investigating stress-strain properties of in-vivo human skin using multiaxial loading experiments and finite element modeling. In: The 26th annual international conference of the IEEE engineering in medicine and biology society. Vol. 2, 2004, p. 5096–9. http://dx.doi.org/10.1109/IEMBS.2004.1404408.

[21] French C, Schultz A, Hajjar J, Shield C, Ernie D, Dexter R, Du C, Olson S, Daugherty D, Wan C. Multi-axial subassemblage testing (MAST) system: description and capabilities. In: 13th world conference on earthquake engineering. WCEE, 2004.

[22] Becerra-Vargas M, Morgado Belo E. Application of H ∞ theory to a 6 DOF flight simulator motion base. J Braz Soc Mech Sci Eng 2012;34(2):193–204. http://dx.doi.org/10.1590/s1678-58782012000200011.

[23] Karimi M, Kosinski C, Brosset L. Comparison of sloshing model test results at scales 1:10 and 1:40. In: Proc. of the 23rd int. offshore and polar engineering conf.. ISOPE, Vol. 3, 2013, p. 224–34.

[24] Han C, Liu K, Ma Y, Qin P, Zou T. Multiaxial fatigue assessment of jacket-supported offshore wind turbines considering multiple random correlated loads. Renew Energy 2021;169:1252–64. http://dx.doi.org/10.1016/j.renene.2021.01.093.

[25] Bufalari G, Van Lieshout PS, Kaminski ML, Den Besten H. Numerical comparative study of multiaxial fatigue methods applied to welded joints in a container vessel. In: 5th symposium on structural durability. SoSDiD, Darmstadt; 2017.

[26] Woudstra J, den Besten H, Seyffert H, Slange R, Donk R. Multiaxial stress response in TLP-type FOWT substructures: an investigation into fatigue assessment of critical weld seams in the time domain (Master's thesis), Delft University of Technology; 2024.
[27] Qin Y, den Besten H, Palkar S, Kaminski ML. Mid- and high-cycle fatigue of welded joints in steel marine structures: Effective notch stress and total stress concept evaluations. Int J Fatigue 2021;142:105822. http://dx.doi.org/10.1016/j.ijfatigue.2020.105822.
[28] Bufalari G, den Besten H, Kaminski ML. Mode-{I, III} multiaxial fatigue of welded joints in steel maritime structures: Effective notch stress based resistance incorporating strength and mechanism contributions. Int J Fatigue 2024;180:108067. http://dx.doi.org/10.1016/j.ijfatigue.2023.108067.
[29] Bufalari G, den Besten H, Hong JK, Kaminski ML. Mode-{I, III} multiaxial fatigue of welded joints in steel maritime structures: Total stress based resistance incorporating strength and mechanism contributions. Int J Fatigue 2024;108499. http://dx.doi.org/10.1016/j.ijfatigue.2024.108499.
[30] Wang L, Qian X, Feng L. Effect of welding residual stresses on the fatigue life assessment of welded connections. Int J Fatigue 2024;189:108570. http://dx.doi.org/10.1016/j.ijfatigue.2024.108570.
[31] Xin H, Correia JA, Veljkovic M, Berto F, Manuel L. Residual stress effects on fatigue life prediction using hardness measurements for butt-welded joints made of high strength steels. Int J Fatigue 2021;147:106175. http://dx.doi.org/10.1016/j.ijfatigue.2021.106175.
[32] Lippardt S. Influence of the geometry on the fatigue strength of welded joints using the effective notch stress approach. Weld World 2022;67(3):669–81. http://dx.doi.org/10.1007/s40194-022-01409-y.
[33] Sedmak S, Burzić Z, Perković S, Jovičić R, Arandelović M, Radović L, Ilić N. Influence of welded joint microstructures on fatigue behaviour of specimens with a notch in the heat affected zone. Eng Fail Anal 2019;106:104162. http://dx.doi.org/10.1016/j.engfailanal.2019.104162.
[34] Zhao J-S, Sun X-C, Wei S-T. Kinematics and statics of the Gough-Stewart platform. Appl Sci (Basel) 2023;13(18):10150.
[35] van Lieshout P. On the assessment of multiaxial fatigue resistance of welded steel joints in marine structures when exposed to non-proportional constant amplitude loading (Ph.D. thesis), TU Delft; 2019, http://dx.doi.org/10.4233/UUID:AFD39F40-7569-4CC6-AC1A-659342B45F9A.
[36] Darcis PP, Lassen T, Récho N. Fatigue behavior of welded joints part 2: Physical modeling of the fatigue process. Weld J 2006;85.
[37] Schork B, Zerbst U, Kiyak Y, Kaffenberger M, Madia M, Oechsner M. Effect of the parameters of weld toe geometry on the FAT class as obtained by means of fracture mechanics-based simulations. Weld World 2020;64(6):925–36. http://dx.doi.org/10.1007/s40194-020-00874-7.
[38] Schubnell J, Jung M, Le CH, Farajian M, Braun M, Ehlers S, Fricke W, Garcia M, Nussbaumer A, Baumgartner J. Influence of the optical measurement technique and evaluation approach on the determination of local weld geometry parameters for different weld types. Weld World 2019;64(2):301–16. http://dx.doi.org/10.1007/s40194-019-00830-0.
[39] Bain E, for Metals AS. Functions of the alloying elements in steel. American Society for Metals; 1939.
[40] Jiang J, Yu Y, Guo Z. Effect of welding heat input on residual stress and crack propagation in Q690CFD welded joints. J Constr Steel Res 2025;226:109297. http://dx.doi.org/10.1016/j.jcsr.2024.109297.
[41] Casagrande A, Cammarota G, Micele L. Relationship between fatigue limit and vickers hardness in steels. Mater Sci Eng: A 2011;528(9):3468–73. http://dx.doi.org/10.1016/j.msea.2011.01.040.
[42] Leonetti D, Maljaars J, Snijder HB. Fracture mechanics based fatigue life prediction for a weld toe crack under constant and variable amplitude random block loading—Modeling and uncertainty estimation. Eng Fract Mech 2021;242:107487. http://dx.doi.org/10.1016/j.engfracmech.2020.107487.
[43] Mikulski Z, Lassen T. Fatigue crack initiation and subsequent crack growth in fillet welded steel joints. Int J Fatigue 2019;120:303–18. http://dx.doi.org/10.1016/j.ijfatigue.2018.11.014.
[44] Otegui J, Burns D, Kerr H, Mohaupt U. Growth and coalescence of fatigue cracks at weld toes in steel. Int J Press Vessels Pip 1991;48:129–65. http://dx.doi.org/10.1016/0308-0161(91)90019-X.
[45] Wormsen A, Sjödin B, Härkegard G, Fjeldstad A. Non-local stress approach for fatigue assessment based on weakest-link theory and statistics of extremes. Fatigue Fract Eng Mater Struct 2007;30(12):1214–27. http://dx.doi.org/10.1111/j.1460-2695.2007.01190.x.
[46] Baumgartner J, Bruder T, Hanselka H. Fatigue strength of laser beam welded automotive components made of thin steel sheets considering size effects. Int J Fatigue 2012;34:65–75. http://dx.doi.org/10.1016/j.ijfatigue.2011.01.022.
[47] Deinböck A, Hesse A-C, Wächter M, Hensel J, Esderts A, Dilger K. Increased accuracy of calculated fatigue resistance of welds through consideration of the statistical size effect within the notch stress concept. Weld World 2020;64:1725–36. http://dx.doi.org/10.1007/s40194-020-00950-y.
[48] Yousefi F, Witt M, Zenner H. Fatigue strength of welded joints under multiaxial loading: Experiments and calculations. Fatigue Fract Eng Mater Struct 2001;24:339–55. http://dx.doi.org/10.1046/j.1460-2695.2001.00397.x.
[49] Luo P, Yao W, Li P. A notch critical plane approach of multiaxial fatigue life prediction for metallic notched specimens. Fatigue Fract Eng Mater Struct 2018;42(4):854–70. http://dx.doi.org/10.1111/ffe.12956.
[50] Schijve J. Biaxial fatigue of metals: the present understanding. Springer International Publishing; 2016, http://dx.doi.org/10.1007/978-3-319-23606-3.
[51] Schijve J. In: Schijve J, editor. Fatigue of structures and materials. Springer Netherlands; 2009.
[52] den Besten H. Fatigue damage criteria classification, modelling developments and trends for welded joints in marine structures. Ships Offshore Struct 2018;13:787–808. http://dx.doi.org/10.1080/17445302.2018.1463609.
[53] den Besten H. Fatigue resistance of welded joints in aluminium high-speed craft: a total stress concept (Ph.D. thesis), Delft University of Technology; 2015, p. 1–396.
[54] Dekking FM, Kraaikamp C, Lopuhaä HP, Meester LE. A modern introduction to probability and statistics: understanding why and how. Springer - Verlag London; 2005, http://dx.doi.org/10.1198/tech.2007.s502.
[55] Qin Y, den Besten H, Palkar S, Kaminski ML. Fatigue design of welded double-sided T-joints and double-sided cruciform joints in steel marine structures: A total stress concept. Fatigue Fract Eng Mater Struct 2019;42:2674–93. http://dx.doi.org/10.1111/ffe.13089.
[56] Sonsino CM. Course of SN-curves especially in the high-cycle fatigue regime with regard to component design and safety. Int J Fatigue 2007;29(12):2246–58. http://dx.doi.org/10.1016/j.ijfatigue.2006.11.015.
[57] Lassen T, Recho N. Proposal for a more accurate physically based S-N curve for welded steel joints. Int J Fatigue 2009;31:70–8. http://dx.doi.org/10.1016/j.ijfatigue.2008.03.032.
[58] Sonsino CM, Kueppers M. Multiaxial fatigue of welded joints under constant and variable amplitude loadings. Fatigue Fract Eng Mater Struct 2001;24:309–27. http://dx.doi.org/10.1046/j.1460-2695.2001.00393.x.
[59] Sonsino CM. Effects on lifetime under spectrum loading. Mater Test 2010;52(7–8):440–51. http://dx.doi.org/10.3139/120.110146.
[60] Ronold KO, Lotsberg I. On the estimation of characteristic S–N curves with confidence. Mar Struct 2012;27(1):29–44. http://dx.doi.org/10.1016/j.marstruc.2012.03.002.
[61] Rother K, Fricke W. Effective notch stress approach for welds having low stress concentration. Int J Press Vessels Pip 2016;147:12–20. http://dx.doi.org/10.1016/j.ijpvp.2016.09.008.
[62] Dong P. A structural stress definition and numerical implementation for fatigue analysis of welded joints. Int J Fatigue 2001;23:865–76. http://dx.doi.org/10.1016/S0142-1123(01)00055-X.
[63] Dong P, Hong JK. The master S-N curve approach to fatigue evaluation of offshore and marine structures. In: 23rd international conference on offshore mechanics and arctic engineering, volume 2. Vol. 2, ASMEDC; 2004, p. 847–55. http://dx.doi.org/10.1115/OMAE2004-51324.
[64] Dong P. A robust structural stress method for fatigue analysis of ship structures. In: Proceedings of the international conference on offshore mechanics and arctic engineering - OMAE. Vol. 3, American Society of Mechanical Engineers Digital Collection; 2003, p. 199–211. http://dx.doi.org/10.1115/OMAE2003-37313.
[65] Qin Y, den Besten H, Palkar S, Kaminski ML. Weld toe and weld root notch induced fatigue of welded joints in steelmarine structures: effective notch stress and total stress concept evaluations. Int J Fatigue 2023.
[66] Fu G, Yang W, Li C-Q. Stress intensity factors for mixed mode fracture induced by inclined cracks in pipes under axial tension and bending. Theor Appl Fract Mech 2017;89:100–9. http://dx.doi.org/10.1016/j.tafmec.2017.02.001.
[67] Predan J, Močilnik V, Gubeljak N. Stress intensity factors for circumferential semi-elliptical surface cracks in a hollow cylinder subjected to pure torsion. Eng Fract Mech 2013;105:152–68. http://dx.doi.org/10.1016/j.engfracmech.2013.03.033.
[68] Sadananda K, Vasudevan AK. Short crack growth and internal stresses. Int J Fatigue 1997;19:99–108.
[69] Sadananda K, Vasudevan A. Crack tip driving forces and crack growth representation under fatigue. Int J Fatigue 2004;26(1):39–47. http://dx.doi.org/10.1016/S0142-1123(03)00105-1.
[70] Sadananda K, Nani Babu M, Vasudevan A. The unified approach to subcritical crack growth and fracture. Eng Fract Mech 2019;212:238–57. http://dx.doi.org/10.1016/j.engfracmech.2019.03.010.
[71] Margetin M, Durka R, Chmelko V. Multiaxial fatigue criterion based on parameters from torsion and axial S-N curve. Frat ed Integrità Strutt 2016;10(37):146–52. http://dx.doi.org/10.3221/igf-esis.37.20.
[72] Hobbacher AF. Recommendations for fatigue design of welded joints and components. IIW collection, Springer International; 2016.
[73] Bibbo ND, Baumgartner J, Arora V. Comparative study of critical plane fatigue criteria on multiaxial variable amplitude loaded welded test specimens. Int J Fatigue 2022;158:106670. http://dx.doi.org/10.1016/j.ijfatigue.2021.106670.
[74] Ng CT, Sonsino CM, Susmel L. Multiaxial fatigue assessment of welded joints: A review of eurocode 3 and international institute of welding criteria with different stress analysis approaches. Fatigue Fract Eng Mater Struct 2024;47:2616–49. http://dx.doi.org/10.1111/ffe.14319.